Two-Tier Frequency-Domain Equalization for Ultra-Wideband Integrated Sensing and Communication

Chao Xu, *Senior Member, IEEE,* Jack Bedwell, Russel N. Torah, Stephen Wang, *Senior Member, IEEE,* Shinya Sugiura, *Senior Member, IEEE,* Robert G. Maunder, *Senior Member, IEEE,* Lie-Liang Yang, *Fellow, IEEE,* Harald Haas, *Fellow, IEEE* and Lajos Hanzo* *Life Fellow, IEEE*

***Abstract*—Ultra-wideband (UWB) radio has license-free access to a substantial bandwidth of over 500 MHz, which makes it a promising candidate for integrated sensing and communication (ISAC), because the performance of both functionalities relies on the availability of sufficient bandwidth. However, due to its regulated power constraint and spectral mask, UWB sensing performance is susceptible to blockage, while the UWB data rate remains low. To enhance both functionalities, we propose a novel two-tier frequency-domain equalization (FDE) scheme for UWB ISAC, in which the first FDE removes the user-specific sequence from the received UWB header in support of sensing, while the second FDE equalizes the effect of channel impulse responses (CIRs) for data detection. The data-carrying amplitude/phase of UWB pulses, which are inherently repeated in the UWB header, naturally follow the circular convolution model without requiring a cyclic prefix (CP) for the proposed sensing operations. Furthermore, the CIRs estimated by the first FDE stage of bistatic sensing can be directly utilized by the second FDE stage of data detection. Compared to the conventional matched filtering (MF) aided UWB sensing, the proposed FDE approach improves the peak-to-sidelobe power ratio and facilitates multi-target sensing. Compared to conventional UWB MF template-based data detection, the proposed approach is capable of improving synchronization, channel estimation and equalization. Furthermore, the proposed two-tier FDE approach inspires a new pulse repetition tradeoff (PR-T) scheme, which reduces pulse repetition to achieve an improved data rate. Our simulation results demonstrate that the proposed UWB FDE sensing achieves centimeter-level accuracy even at a low Ricean K-factor of -4 dB. Additionally, the proposed FDE data detection designed for PR-T is capable of improving the UWB data rate from the single Megabits-per-second (Mbps) range to over 100 Mbps, at the cost of reduced pulse repetition gain.**

***Index Terms*—Ultra-wideband, UWB, impulse radio, integrated sensing and communication, ISAC, frequency-domain equalization, FDE, cyclic prefix, CP, index modulation, OFDM, bistatic, two-way ranging.**

C. Xu, J. Bedwell, R. N. Torah, R. G. Maunder L-L. Yang and L. Hanzo are with the School of Electronics and Computer Science, University of Southampton, Southampton SO17 1BJ, UK (e-mail: {cx1g08,jb4n21,rnt,rm,lly,lh}@soton.ac.uk). S. Wang is with VIAVI Marconi Labs, VIAVI Solutions Inc., Stevenage SG1 2AN, UK (e-mail: stephen.wang@viavisolutions.com). S. Sugiura is with the Institute of Industrial Science, University of Tokyo, Meguro-ku, Tokyo 153-8505, Japan (e-mail:sugiura@ieee.org). H. Haas is with the Department of Engineering, Electrical Engineering Division, Cambridge University, Cambridge CB3 0FA, UK (e-mail:huh21@cam.ac.uk).

The work of S. Sugiura was supported in part by the Japan Science and Technology Agency (JST) ASPIRE under Grant JPMJAP2345. L. Hanzo would like to acknowledge the financial support of the Engineering and Physical Sciences Research Council (EPSRC) projects under grant EP/X01228X/1, EP/Y026721/1, EP/W032635/1, EP/Y037243/1, EP/X04047X/1 and EP/W032635/1.

I. Introduction

Integrated sensing and communication (ISAC) is expected to be a cornerstone technology for 6G [1]–[4]. Reliable localization and Internet access in diverse indoor and outdoor environments offer significant benefits for applications, such as navigation in underground and large buildings, supporting firefighters in search and rescue operations, tracking Internet of things (IoT) devices, and assisting vulnerable individuals. However, the heavily congested 5G and WiFi bands present a significant bottleneck. For instance, 5G positioning, which relies on positioning and sounding reference signals, can only achieve an accuracy of about 1 meter indoors and 10 meters outdoors [5]. Additionally, satellite-based Global Positioning System (GPS) signals are prone to severe degradation from multipath propagation in urban street-canyons and exhibit poor building-penetration. Given these limitations, ultra-wideband (UWB) radio emerges as a promising candidate for short-range ISAC, thanks to its license-free access to a substantial bandwidth of over 500 MHz.

UWB systems are unlicensed yet regulated, meaning their operations must adhere to regulated frequency and power ranges [6], [7]. Consequently, despite their similar impulse radio transmissions, UWB operations [8]–[13] are considerably different from pilot-based channel estimation using Dirac delta signals [14]–[16]. In pilot-based channel estimation, the Dirac delta signals experience both a direct propagation delay τ_0 and multipath channel impulse responses (CIRs) $\{h_l\}_{\forall l}$, as portrayed by Fig. 1a). Synchronization based on the estimated delay $\hat{\tau}_0$ can be achieved through energy detection, after which the estimated CIR taps $\{\hat{h}_l\}_{\forall l}$ can be read one-by-one. In contrast, UWB impulse radio exhibits three distinct features, as illustrated in Fig. 1b). First, due to their high bandwidth, UWB typically transmits narrower pulses, making multipath components more resolvable. Second, due to regulatory constraints, the UWB pulses are weaker in power, which necessitates repeating the pulses multiple times. This repetition allows the UWB correlation-based matched filter (MF) receiver to accumulate multipath powers across all repeated pulses, resulting in a beneficial pulse repetition gain. Third, since UWB pulses may be too weak to bounce back for monostatic sensing, often two-way ranging is used, where the transmitter calculates the round-trip duration based on the time-stamp responded by the receiver. This method eliminates the need for strict clock synchronization [6], [7].

Due to their license-free access, UWB systems have be-

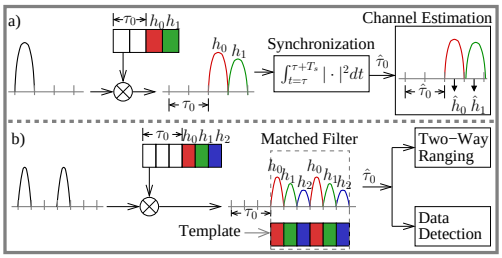

Fig. 1: Impulse radio for a) pilot-aided channel estimation, b) UWB ISAC.

come popular for ISAC applications in recent years [17]–[23]. Firstly, a variety of research institutions and companies have experimented with UWB ISAC applications, including low-power/low-cost beamforming schemes for communication [17]–[19], multiple signal classification (MUSIC) for sensing [20], [21] and Kalman filtering for tracking [22], [23]. Secondly, as early as 2007, the IEEE 802.15.4a amendment incorporated both low-data-rate wireless communication and high-precision ranging using UWB techniques [6]. To improve the UWB data rate, the IEEE 802.15.4f amendment proposed a pair of UWB modes in 2012, where the high-rate pulse (HRP) mode transmits more pulses at a lower power, while the low-rate pulse (LRP) mode transmits less pulses at higher power [6], [24]. Recently, the IEEE 802.15.4z standard, released in 2020, included enhancements such as improved channel coding and preamble designs [24], [25]. Thirdly, regarding commercialization efforts, both Apple and Samsung have deployed UWB schemes for nearby environment awareness and interactions [26], [27]. The Car Connectivity Consortium (CCC) is working on UWB-based keyless access and location-aware features for vehicles [28]. The FiRa Consortium, supported by key UWB players such as Qorvo, NXP Semiconductors, HID Global and Bosch, provides certificates for interoperable UWB devices that comply with the IEEE 802.15.4/4z standards [29].

However, due to the power constraints, the UWB sensing performance is susceptible to blockage, while the UWB data rate remains low. Generally, there are three types of UWB MF receivers [8]–[11]. Firstly, the line-of-sight (LoS) based UWB directly utilizes the user-specific time-hopping sequence as its MF receiver's correlation template [8]. Secondly, the training-based UWB relies on the so-called "clean template" of aggregate receive-pulse [9], [10], which must be obtained through training. A sensing peak is detected, when the template is synchronized with the multipath components of the received pulses, as portrayed by Fig. 1b). Thirdly, the blind "dirty template" method of [11] directly utilizes the data-carrying received pulses, where sensing peaks are detected based on the Cauchy-Schwarz inequality. Although the training-based and blind UWB schemes are more robust in multipath scenarios than the LoS-based scheme, none of the UWB MF sensing methods achieve orthogonality between the sensing peaks and sidelobes. The sidelobes are never zero, even in ideal noise-free conditions, and the peak-to-sidelobe ratio significantly decreases in the face of blockages.

It is widely recognized that orthogonal frequency-division multiplexing (OFDM) radar [30]–[32] based on fast Fourier transform (FFT) and inverse FFT (IFFT) is capable of suppressing sidelobes and enabling multi-target sensing. However, the current UWB impulse radio standards and commercial products generally rely on the linear convolution model and operate without cyclic prefix (CP), rather than harnessing OFDM's circular convolution model. An exception is the multi-band (MB) OFDM designed for UWB communication [33], [34], where a subset of subcarriers is activated to convey low-power, low-rate UWB signals. However, MB-OFDM schemes have the disadvantage of high peak-to-average power ratio (PAPR) and the lack of pulse repetition gain. Recently, the coupling between UWB sensing's delay detection and pulse position modulation (PPM) data detection was investigated in [35]–[39]. Specifically, a soft-information-based UWB ISAC decoupling solution was conceived in [39], and a Kalman filter was used for smoothing the trajectory of user movement. However, in [39], the UWB MF receiver used the transmitter's pulse template without pulse repetition gain, where the FFT/IFFT was applied without accounting for the extra cost of the CP. The CP duration for ISAC has to cover both propagation delay and delay spread [30]–[32], resulting in a long CP duration that may become equivalent to a symbol duration. This further reduces the UWB data rate by half.

Against this background, we propose a novel two-tier frequency-domain equalization (FDE) scheme for UWB ISAC. The original FDE was designed for removing CIRs for data detection, but here we extend this concept to removing user-specific time-hopping sequence from UWB header for sensing. The key contributions of this work, highlighted in comparison to the state-of-the-art in Table I, are detailed as follows:

- We propose to exploit the inherent UWB symbol repetition pattern in both training-based and blind sensing methods, where a subset of UWB symbols naturally follow the circular convolution model, without requiring a CP. Based on this, we conceive a single-tap FDE method for removing the user-specific time-hoping sequence from the received UWB header, after which Fourier-transform-based sensing operation is performed. Compared to the conventional MF aided UWB sensing [8]–[11], OFDM ISAC [30]–[32] and decoupling-based UWB ISAC [35]–[39], the proposed UWB FDE sensing stage is capable of achieving peak-sidelobe orthogonality and multi-target sensing without altering the UWB header format.
- To avoid coupling between delay detection and PPM data detection encountered in [35]–[39], PPM is de-activated for UWB sensing header operating in the LRP mode, but it is still activated for the UWB data payload in the HRP mode. As a result, the UWB header's delay detection and data detection are mutually independent, which facilitates the employment of high-order pulse amplitude modulation (PAM), phase shift keying (PSK), or quadrature amplitude modulation (QAM) constellations that improve the data rate of UWB header.
- Furthermore, we propose a second single-tap FDE to equalize the CIRs for detecting the UWB data payload. Unlike conventional UWB channel estimation schemes [12], [13] and noncoherent UWB schemes [40]–[42], our proposed two-tier ISAC scheme enables the second stage of UWB data detection to directly utilize the estimated CIRs obtained from the first stage of UWB FDE-based

TABLE I: Novel contributions of this work in comparison to state-of-the-art.

	UWB Sensing Header				UWB Data Payload				
	Pulse repetition design?	Peak-sidelobe orthogonality?	Multi-target?	Extended to PAM/PSK/QAM?	Pulse repetition design?	FDE ISI-free?	Channel estimation?	Higher throughput than UWB PPM?	Single-stream detection?
LoS-based UWB Sensing [8]	√				√				√
Training UWB Sensing [8]–[10]	√				√		√		√
Blind UWB Sensing [11]	√				√				√
UWB Channel Estimation [12], [13]	√				√		√		√
Noncoherent UWB Commun. [40]–[42]	√				√				√
UWB MB-OFDM Commun. [33], [34]						√	√	√	√
Index modulation Commun. [43]–[45]						√	√	√	√
OFDM ISAC [30]–[32]		√	√	√		√	√	√	√
Decoupling UWB ISAC [35]–[39]			√				√		√
Proposed FDE aided UWB ISAC	√	√	√	√	√	√	√	√	√

sensing. Compared to conventional UWB MF template-based data detection [8]–[13], index modulation [43]–[45] and OFDM-based communication schemes [30]–[34], our proposed approach is capable of better synchronizing, estimating and equalizing the CIRs.

- Although no CP is required for the first FDE aided UWB sensing header, it remains necessary for the second FDE aided UWB data payload. However, synchronization can be performed based on UWB header before processing UWB data payload. To ensure a circular convolution model for the UWB payload, we propose to copy the last pulse of each UWB payload symbol and place it at the front as CP. This results in a low CP percentage while preserving the UWB payload's duty cycle.
- In order to further improve the data rate of UWB payload, we propose a novel pulse repetition tradeoff (PR-T) based scheme that resembles the principle of index modulation [43]–[45] along with FDE, where more PPM indices are modulated within a UWB symbol, at the cost of a reduced pulse repetition gain.
- Our simulation results demonstrate that the proposed FDE for UWB sensing header is capable of achieving centimeter-level sensing accuracy even at a low Ricean K-factor of -4 dB, where conventional UWB MF sensing methods exhibit excessive errors. Furthermore, for an UWB system having a bandwidth of $B_c = 512$MHz, a pulse repetition frequency of $B_G = 64$MHz and a CP percentage of $1/65$, the proposed PR-T scheme is capable of improving the achievable rate of the UWB payload from 2Mbps to 7.875Mbps, 31.5Mbps and 126Mbps, when the pulse repetition gain is reduced from $\ddot{G}_R = 64$ to $\ddot{G}_R = 16$, $\ddot{G}_R = 4$ and $\ddot{G}_R = 1$, respectively.

The paper is organized as follows. The UWB ISAC model is presented in Sec. II. The proposed UWB sensing and data detection methods are presented in Sec. III and Sec. IV, respectively. Our simulation results are presented in Sec. V, and our conclusions are offered in Sec. VI.

II. UWB ISAC System Model

In this section, the UWB ISAC system is introduced in Sec. II-A, while the transmission and reception models are discussed in Sec. II-B and Sec. II-C, respectively.

A. System Description

Fig. 2 illustrates the UWB ISAC system model using a two-way ranging protocol. First of all, a poll signal, consisting of a UWB header and payload, is sent by the tag to the anchor. The UWB header operates in LRP mode to support both

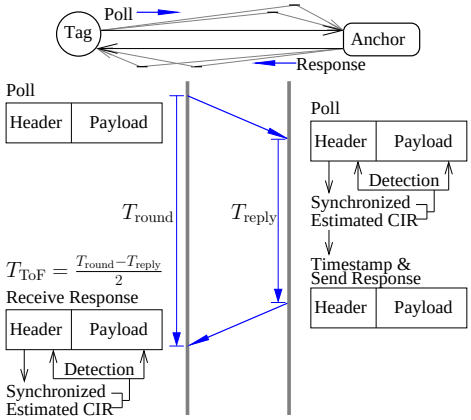

Fig. 2: Schematic of UWB ISAC model with two-way ranging.

sensing and low-rate communication, while the UWB payload operates in HRP mode for high-rate communication. Secondly, upon receiving the delayed and multipath-contaminated poll signal, the anchor first performs sensing on the UWB header, which provides synchronization and CIR estimations for data detection in both the UWB header and payload. The anchor then records its timestamp based on its local clock and sends a response back to the tag. Finally, the tag receives the response and performs its own sensing and data detection. The estimation on time-of-flight (ToF) is given by $T_{\text{TOF}} = \frac{T_{\text{round}} - T_{\text{reply}}}{2}$, where T_{reply} and T_{round} refer to the anchor's reply time recorded in the anchor's time-stamp and the round-trip time estimated by the tag, respectively. Therefore, the distance between the anchor and the tag can be estimated by $d = cT_{\text{TOF}}$, where c represents the speed of light.

The two-way ranging depicted by Fig. 2 offers several benefits for UWB ISAC. Firstly, the two bistatic sensing steps mimic monostatic sensing without requiring the signals to be reflected back to the transmitter by the target. Secondly, due to the use of timestamp, clock synchronization between the tag and the anchor is no longer necessary. Thirdly, channel estimation for data detection can be directly performed by the receiver in each bistatic sensing step. Without loss of generality, we proceed to investigate one-way UWB transmission and reception in a single bistatic step, which applies to both the poll and response phases in Fig. 2.

B. Modulation and Parameters

The modulation of UWB impulse radio is based on both PAM/PSK/QAM and PPM [8]–[10]:

$$\begin{aligned} s(t) &= \sqrt{\epsilon}\sum_{n=-\infty}^{\infty} a_n \sum_{g=0}^{G-1} p(t - nT_S - gT_G - c_g T_c - b_n T_c \Delta) \\ &= \sum_{n=-\infty}^{\infty} a_n p_{\text{Tx}}(t - nT_S - b_n T_c \Delta), \end{aligned} \tag{1}$$

where the complex-valued a_n and real-valued non-negative integers b_n are pulse amplitude/phase and pulse position, modulated by PAM/PSK/QAM and PPM, respectively, while ϵ and $p(\cdot)$ denote transmit power and pulse function, respectively. The transmit waveform template is defined by $p_{\text{Tx}}(t) = \sqrt{\epsilon}\sum_{g=0}^{G-1} p(t-gT_G-c_gT_c)$. The series of $\{c_g\}_{g=0}^{G-1}$ represents a psudo-random user-specific time-hopping sequence. A predetermined delay Δ is chosen to maximize the separation between PPM indices.

In (1), an UWB symbol contains M chips, which are arranged into G groups. Within each group of $M_G = \frac{M}{G}$ chips, only a single pulse position is activated. The corresponding symbol duration, pulse repetition interval (PRI) and chip duration are given by $T_S = \frac{1}{B_S}$, $T_G = \frac{1}{B_G}$ and $T_c = \frac{1}{B_c}$, respectively, where B_S, B_G and B_c denote symbol rate, pulse repetition frequency (PRF) and chip rate, respectively. Therefore, the total number of pulses per symbol is characterized by $G = \frac{T_S}{T_G} = \frac{B_G}{B_S}$, and the total number of chips per PRI is given by $M_G = \frac{T_G}{T_c} = \frac{B_c}{B_G}$. For example, in a classic UWB system with a bandwidth of $B_c = 512$MHz and a symbol rate of $B_S = 1$MHz, there are $M = 512$ chips within a UWB symbol duration. The symbol duration and chip duration are $\frac{1}{B_S} = 1\mu$s and $\frac{1}{B_c} \approx 2$ns, respectively, which indicate that the maximum sensing range and sensing resolution are $\frac{c}{B_S} = 300$m and $\frac{c}{B_c} \approx 0.6$m, respectively. The resolution of 0.6m indicates that the maximum error can be 0.3m. If we consider the sensing error to be uniformly distributed between 0 and 0.3m, the average sensing error is expected to be 0.15m, which aligns with the UWB general performance of centimeter-level sensing accuracy [46].

The discrete-time representation of (1) is expressed as:

$$s_{n,m}=\sqrt{\epsilon}a_n\textstyle\sum_{g=0}^{G-1}\delta(m-gM_G-c_g-b_n\Delta)=a_n\beta^{\text{Tx}}_{m-b_n\Delta}, \quad (2)$$

where $\delta(\cdot)$ refers to a Dirac delta function, while the subscripts for $s_{n,m}$ refer to the n-th symbol's m-th chip, and the transmit-pulse template in discrete-time is defined by $\beta^{\text{Tx}}_m = \sqrt{\epsilon}\sum_{g=0}^{G-1}\delta(m-gM_G-c_g)$.

C. Received Signal Model

The UWB received signal model is given by [8]–[10]:

$$\begin{aligned} y(t) &= \textstyle\sum_{n=-\infty}^{\infty}\sum_{p=0}^{P-1} h_p s(t-\tau_p) + v(t) \\ &= \textstyle\sum_{n=-\infty}^{\infty} a_n p_{\text{Rx}}(t-nT_S-b_nT_c\Delta-\tau_0) + v(t), \end{aligned} \quad (3)$$

where $v(t)$ refers to the additive white Gaussian noise (AWGN) with zero mean and variance of N_0, while the aggregate receive-pulse template is defined by $p_{\text{Rx}}(t) = \sqrt{\epsilon}\sum_{p=0}^{P-1} h_p p_{\text{Tx}}(t-\tau_{p,0})$ and we have $\tau_{p,0} = \tau_p - \tau_0$. Let us assume that there are P CIR taps $\{h_p\}_{p=0}^{P-1}$ and their delays are given by $\{\tau_p\}_{p=0}^{P-1}$. The first tap associated with $p = 0$ is the LoS path and the rest associated with $1 \le p \le P-1$ are non-LoS (NLoS) paths. The power ratio between the LoS and NLoS paths is featured by the Ricean K-factor of $K = E\left\{\frac{|h_0|^2}{\sum_{p=1}^{P-1}|h_p|^2}\right\}$. More explicitly, the LoS path is modelled by $h_0 = \sqrt{\frac{K}{K+1}}\text{PL}$, where the path loss (PL) is given by $\text{PL} = \sqrt{\frac{\lambda^2 G_{\text{Tx}} G_{\text{Rx}}}{(4\pi)^2 d^2}}$ [32]. We note that $\lambda = \frac{c}{f_c}$, $c = 3\times10^8$ and f_c represent the wavelength, speed of light and carrier frequency, respectively. The transmit and receive antenna gains are given by $G_{\text{Tx}} = \frac{4\pi A_{\text{Tx}}}{\lambda^2}$ and $G_{\text{Rx}} = \frac{4\pi A_{\text{Rx}}}{\lambda^2}$, respectively, where A_{Tx} and A_{Rx} are transmit and receive antenna apertures, respectively. The LoS delay is given by $\tau_0 = \frac{d}{c}$, where d is the distance between the transmitter and receiver. The NLoS paths are modelled by $\{h_p \in \mathcal{CN}(0, \frac{\text{PL}}{(K+1)(P-1)})\}_{p=1}^{P-1}$, where $\mathcal{CN}(0, \frac{\text{PL}}{(K+1)(P-1)})$ denotes the complex Gaussian distribution with zero mean and a variance of $\frac{\text{PL}}{(K+1)(P-1)}$. The NLoS delays $\{\tau_p\}_{p=0}^{P-1}$ are randomly generated between τ_0 and T_S.

The discrete-time representation of (3) is given by:

$$\begin{aligned} y_{n,m} &= \textstyle\sum_{n'=n-1}^{n}\sum_{p=0}^{P-1} h_p s_{n',m-l_p} + v_{n,m} \\ &= \textstyle\sum_{n'=n-1}^{n} a_{n'}\beta^{\text{Rx}}_{m-b_n\Delta-l_0} + v_{n,m}, \end{aligned} \quad (4)$$

where $\{l_p = \frac{\tau_p}{T_c}\}_{p=0}^{P-1}$ are delay indices, while the n-th symbol will only receive ISI from the $(n-1)$-th symbol for short-range UWB with small delay spread, i.e. $l_{P-1} << M$. The discrete-time aggregate receive-pulse template is defined by $\beta^{\text{Rx}}_m = \sum_{p=0}^{P-1} h_p \beta^{\text{Tx}}_{m-l_{p,0}}$, where we have $l_{p,0} = l_p - l_0$. Moreover, we note that due to the low-power, short-range nature of UWB radio, the Doppler frequency is not modelled in (3) and (4). For instance, at a pedestrian speed of 3.2mph, a UWB system operating at a carrier frequency of $f_c = 7$GHz experiences a maximum Doppler frequency of 33.13Hz. This value is negligible compared to both the 1MHz symbol rate and 512MHz bandwidth discussed in Sec. II-B.

III. UWB Sensing Header: How to Achieve Peak-Sidelobe Orthogonality?

In this section, the received UWB header is modelled in Sec. III-A. The conventional training-based, blind and LoS-based UWB MF sensing methods are presented in Sec. III-B, Sec. III-C and Sec. III-D, respectively, while their transformation from the linear convolution model to the circular convolution model is proposed in Sec. III-E. The UWB FDE sensing receiver is presented in Sec. III-F, and the data detection in the UWB header is portrayed in Sec. III-G.

A. Received Sensing Signal Model

For the UWB header, PPM is de-activated in order to avoid coupling between sensing and PPM. Therefore, we have $b_n = 0$ in (2) and (4). It can be observed that the first non-zero pulse associated with index $m = c_0$ transmitted based on (2) is shifted to $m = l_0 + c_0$ in the received signal model of (4). More explicitly, the received signal of (4) can be extended as:

$$\begin{aligned} y_{n,m} &= \sqrt{\epsilon}a_n \textstyle\sum_{\forall p\in\{l_p\le m\}} h_p \sum_{g=0}^{G-1}\delta(m-gM_G-c_g-l_p) \\ &+\sqrt{\epsilon}a_{n-1}\textstyle\sum_{\forall p\in\{l_p>m\}} h_p\sum_{g=0}^{G-1}\delta(m-gM_G-c_g-l_p+M)+v_{n,m}, \end{aligned} \quad (5)$$

where the second term associated with a_{n-1} introduces inter-symbol interference (ISI). In order to avoid ISI at the target index $m = l_0 + c_0$, it is sufficient to ensure that we have $c_0 - (G-1)M_G - c_{G-1} - l_{p,0} + M > 0$ for the ISI term. This sufficient condition can be expressed by $c_0 \ge c_{G-1}$ and $M_G \ge l_{p,0} + 1$. Based on this, the received signal of (5) associated with $0 \le m < l_0 + c_0$ has the first term that carries a_n equal to zero, due to the index range of $m - gM_G - c_g - l_p < c_0 - c_g - gM_G - l_{p,0} \le 0$. Similarly, for the received signal of (5) associated with $l_0 + c_0 \le m < M$, the second term that carries a_{n-1} equals to zero, due to the index range of

$m - gM_G - c_g - l_p + M \geq c_0 - c_g + M - gM_G - l_{p,0} \geq c_0 - c_{G-1} + M_G - l_{p,0} > 0$. In summary, when we have $c_0 \geq c_{G-1}$ and $M_G \geq l_{p,0} + 1$, (5) can be expressed as (6), where the target delay index is given by $l'_0 = l_0 + c_0$.

B. Training-Based UWB Sensing

If the clean aggregate receive-pulse template $\{\beta^{\text{Rx}}_{m-l'_0}\}^{M}_{m=0}$ is perfectly known, the sensing peak can be detected by the MF's correlation operation $\sum_{m=l}^{M+l-1} y_{n,m}(\beta^{\text{Rx}}_{m-l'_0})^*$, where the correlation window spanning from $m = l$ to $M + l - 1$ shifts with the variable index l. The search range is given by $0 \leq l \leq M - 1$ [8]–[10]. Specifically, for the range of $l < l'_0$, the correlation metric is given by (7). We note that the chip index m is not confined within the range of $[0, M - 1]$ in (7) for the convenience of the linear convolution model. Explicitly, based on the notation definition of $t = (nM + m)T_c$ in (2) and (4), we have $s_{n,m} = s_{n+1,m-M}$ and $y_{n,m} = y_{n+1,m-M}$ for $M \leq m \leq M + l - 1$ utilized in (7). It can be observed in (7) that the correlation window may contain non-zero ISI terms associated with a_{n-1}.

Secondly, for the case of $l = l'_0$ at the target index, the correlation metric of (7) can be simplified based on (6) as:

$$\sum_{m=l'_0}^{M+l'_0-1} y_{n,m}(\beta^{\text{Rx}}_{m-l'_0})^* \overset{*}{=} a_n \sum_{m=0}^{M-1} \left|\beta^{\text{Rx}}_{m-l'_0}\right|^2 + \sum_{m=l'_0}^{M+l'_0-1} v_{n,m}(\beta^{\text{Rx}}_{m-l'_0})^*, \tag{8}$$

which does not contain ISI and hence a sensing peak is formed.

Finally, for the range of $l > l'_0$, the correlation metric of (7) is given by (9), which contains ISI term associated with a_{n+1}.

Ideally, the correlation metric $\sum_{m=l}^{M+l-1} y_{n,m}(\beta^{\text{Rx}}_{m-l'_0})^*$ is peaked at $l = l'_0$. However, the correlation metric of (8) at $l = l'_0$ may not be the only peak, because the ISI terms in (7) may occasionally be zero. In other words, the sufficient condition for the case of $l = l'_0$ of (8) to be the only peak is that the ISI term in (7) must be non-zero, i.e. we have the index of $m - gM_G - c_g - l_p + M = 0$. For the special case of $m = l'_0 - 1$, the condition of $l'_0 - 1 - gM_G - c_g - l_p + M = 0$ requires $c_0 = c_{G-1}$ and $M_G = l_{p,0} + 1$, which limits the choices of time-hopping sequences and requires a prior knowledge of the delay spread. Without these stringent conditions, the case of $l = l'_0$ of (8) will always be the last peak before a series of sidelobes, where peaks capture all multipath powers associated with $\{h_{l'_0}, \cdots, h_{l'_{P-1}}\}$ for a_n in (8). When the window is shifted to the sidelobe region of $l > l'_0$, the multipath powers associated with $\{h_{l'_0}, \cdots, h_{l-1}\}$ for a_n are missed in (9), leading to a reduced correlation metric value. Therefore, this transition from the peak to sidelobe is targeted for detection.

Moreover, the template $\{\beta^{\text{Rx}}_{m-l'_0}\}^{M}_{m=0}$ has to be estimated based on N_1 training symbols [9], [12], [13]:

$$\hat{\beta}^{\text{Rx}}_{m-l'_0} = \tfrac{1}{N_1} \sum_{n=1}^{N_1} y_{n,m}, \tag{10}$$

where $a_n = 1$ for training. The first transmission associated with $n = 0$ is not used in (10), because it does not capture the ISI pattern, i.e. there is no a_n associated with $n = -1$.

In summary, the MF's correlation metric is given by:

$$J_l = \tfrac{1}{N} \sum_{n=N_1+1}^{N_1+N} \left|\sum_{m=l}^{M+l-1} y_{n,m}(\hat{\beta}^{\text{Rx}}_{m-l'_0})^*\right|^2. \tag{11}$$

The target index l'_0 is detected as the last peak before sidelobes, i.e. $\hat{l}'_0 = \max\ \forall\{\bar{l}\}$, where $\{\bar{l}\}$ is the set of indices of the peaks, i.e. $J_{\bar{l}} = J_{\max} = \max_{\forall l=0,\cdots,M-1}\ J_l$. Once the target l'_0 is missed, the correlation metric becomes smaller. This transition can be expressed as $J_{\hat{l}'_0} = J_{\max}$ and $J_{\hat{l}'_0+1} < J_{\hat{l}'_0}$.

C. Blind UWB Sensing

Upon dispensing with the training overhead, the blind UWB scheme operates based on the Cauchy-Schwarz inequality [11]:

$$\left|\sum_{m=l}^{M+l-1} y_{n,m} y^*_{n+1,m}\right|^2 \leq \left(\sum_{m=l}^{M+l-1} |y_{n,m}|^2\right)\left(\sum_{m=l}^{M+l-1} |y_{n+1,m}|^2\right), \tag{12}$$

where the equality of the above equation holds at $l = l'_0$ with $\left\{\frac{y_{n+1,m}}{y_{n,m}} = \frac{a_{n+1}}{a_n}\right\}_{m=l'_0}^{M+l'_0-1}$ for the noise-free version of received signal model of (6). Therefore, the MF's correlation metric can be expressed as:

$$J_l = \tfrac{1}{N} \sum_{n=1}^{N} \left|\sum_{m=l}^{M+l-1} y_{n,m} y^*_{n+1,m}\right|^2. \tag{13}$$

Accordingly, the target $\hat{l}'_0$ is detected as the index of the last peak before sidelobes, i.e. $J_{\hat{l}'_0} = J_{\max} = \max_{\forall l=0,\cdots,M-1}\ J_l$ and $J_{\hat{l}'_0+1} < J_{\hat{l}'_0}$. For the sake of quick convergence, the preamble data are modulated in the form of $(a, a, -a, -a)$, i.e. $\{a_{4i-3} = a_{4i-2} = -a_{4i-1} = -a_{4i}\}_{i=1}^{\frac{N}{4}}$, so that ISI will be destructively superimposed at sidelobes.

D. LoS-Based UWB Sensing

When the LoS dominates signal reception, the received signal model of (4) is simplified to:

$$y_{n,m} = \sum_{p=0}^{P-1} h_p s_{n,m-l_p} + v_{n,m} \approx h_0 s_{n,m-l_0} + v_{n,m}. \tag{14}$$

Based on the LoS model, the transmit-pulse template is sufficient for detecting sensing peaks, where the MF's correlation metric is given by:

$$J_l = \tfrac{1}{N} \sum_{n=1}^{N} \left|\sum_{m=l}^{M+l-1} y_{n,m} \beta^{\text{Tx}}_{m-l}\right|^2. \tag{15}$$

E. How to Transform the UWB Linear Convolution Model to Circular Convolution Model?

The classic UWB impulse radio technology relies on the pulse repetition design and obeys the linear convolution model, where FFT/IFFT cannot be directly applied. These principles have been overlooked by many recent UWB ISAC publications [35]–[39]. In order to better understand this, we portray some examples of the UWB MF sensing methods in Fig. 3. Firstly. the UWB modulation in Fig. 3 has $M = 6$ chips for each UWB symbol, where each PAM/PSK/QAM-modulated pulse $\{a_n\}$ is repeated $G = 2$ times. Secondly, the transmitted pulses are delayed and spread by $P = 3$ paths associated with delay indices of $l_0 = 2$, $l_1 = 3$ and $l_2 = 4$, as exemplified by Fig. 3. Thirdly, the LoS-based UWB MF sensing method utilizes the transmit-pulse template. A peak is detected, when the activated pulse positions in the template match the delayed pulses received through LoS paths, as seen in Fig. 3. By contrast, the training-based UWB MF sensing method utilizes a clean aggregate receive-pulse template. A sensing peak is detected, where there is no ISI within the MF's correlation window. Moreover, the blind UWB MF sensing method utilizes a "dirty" template that contains data. A peak is detected, when two segments in the received signals are synchronized based on the Cauchy-Schwarz inequality.

$$y_{n,m}=\begin{cases}\sqrt{\epsilon}a_{n-1}\sum_{\forall p\in\{l_p>m\}}h_p\sum_{g=0}^{G-1}\delta(m-gM_G-c_g-l_p+M)+v_{n,m}, & \text{if } 0\le m<l_0'\\ \sqrt{\epsilon}a_n\sum_{\forall p\in\{l_p\le m\}}h_p\sum_{g=0}^{G-1}\delta(m-gM_G-c_g-l_p)+v_{n,m}, & \text{if } l_0'\le m<M\end{cases}, \tag{6}$$

$$\begin{aligned}\sum_{m=l}^{M+l-1}y_{n,m}(\beta_{m-l_0'}^{\text{Rx}})^*=\ &\epsilon a_{n-1}\sum_{m=l}^{l_0'-1}\left|\sum_{\forall p\in\{l_p>m\}}h_p\sum_{g=0}^{G-1}\delta(m+M-gM_G-c_g-l_p)\right|^2\\ &+\epsilon a_n\sum_{m=l_0'}^{M-1}\left|\sum_{\forall p\in\{l_p\le m\}}h_p\sum_{g=0}^{G-1}\delta(m-gM_G-c_g-l_p)\right|^2\\ &+\epsilon a_n\sum_{m=M}^{M+l-1}\left|\sum_{\forall p\in\{l_p>m-M\}}h_p\sum_{g=0}^{G-1}\delta(m-gM_G-c_g-l_p)\right|^2+\sum_{m=l}^{M+l-1}v_{n,m}(\beta_{m-l_0'}^{\text{Rx}})^*.\end{aligned} \tag{7}$$

$$\begin{aligned}\sum_{m=l}^{M+l-1}y_{n,m}(\beta_{m-l_0'}^{\text{Rx}})^*=&\epsilon a_n\sum_{m=l}^{M-1}\left|\sum_{\forall p\in\{l_p\le m\}}h_p\sum_{g=0}^{G-1}\delta(m-gM_G-c_g-l_p)\right|^2\\ &+\epsilon a_n\sum_{m=M}^{M+l_0'-1}\left|\sum_{\forall p\in\{l_p>m-M\}}h_p\sum_{g=0}^{G-1}\delta(m-gM_G-c_g-l_p)\right|^2\\ &+\epsilon a_{n+1}\sum_{m=M+l_0'}^{M+l-1}\left|\sum_{\forall p\in\{l_p\le m-M\}}h_p\sum_{g=0}^{G-1}\delta(m-gM_G-c_g-l_p-M)\right|^2+\sum_{m=l}^{M+l-1}v_{n,m}(\beta_{m-l_0'}^{\text{Rx}})^*,\end{aligned} \tag{9}$$

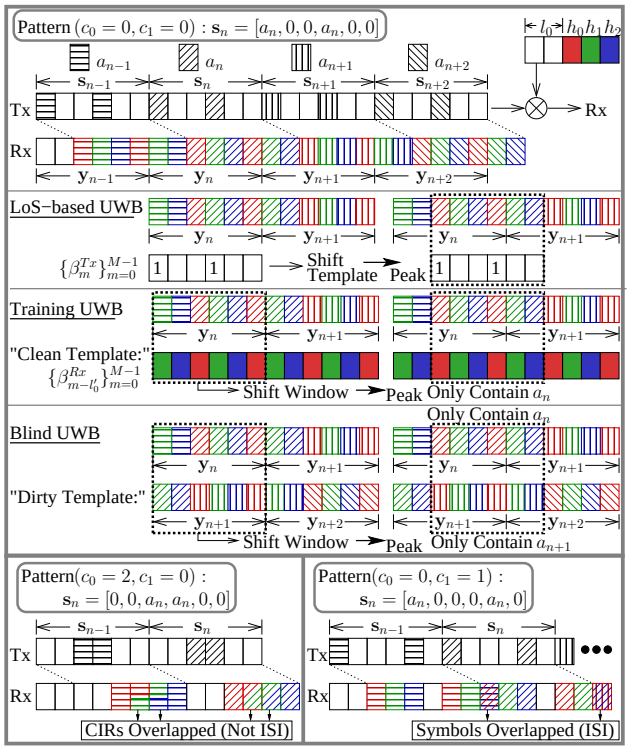

Fig. 3: Examples of UWB MF sensing methods.

For the parameters of $M=6$ and $G=2$, there are nine possible patterns for the user signature (c_0,c_1), where $\{0\le c_g\le M_G-1\}_{g=0,1}$. As discussed in Sec. III-B, the conditions of $c_0\ge c_{G-1}$ and $M_G\ge l_{p,0}+1$ have to be satisfied for ensuring that the target delay indices c_0+l_0 are free of ISI. For the case of $(c_0=2,c_1=0)$ in Fig. 3, the CIR taps are overlapped for the repeated pulses, which does not impose ISI. Therefore, the UWB MF detection of $(c_0=0,c_1=0)$ is applicable to $(c_0=2,c_1=0)$ in Fig. 3. However, for the case of $(c_0=0,c_1=1)$ in Fig. 3, the CIR taps are overlapped for the pulses from different symbols, which lead to ISI. In summary, three user signature patterns of $(c_0=0,c_1=1)$, $(c_0=0,c_1=2)$ and $(c_0=1,c_1=2)$ should be eliminated for UWB MF-based sensing.

Fig. 3 demonstrates that there is no orthogonality between the sensing peaks and sidelobes. The sidelobes are never zero, not even in idealistic noise-free scenarios, hence the peak-to-sidelobe ratio is highly dependent on the LoS power. Against this background, we propose to exploit the inherent UWB symbol repetition patterns in sensing signals. As exemplified by Fig. 4, the training-based UWB transmits N_1 identical training symbols, where one training symbol naturally acts as

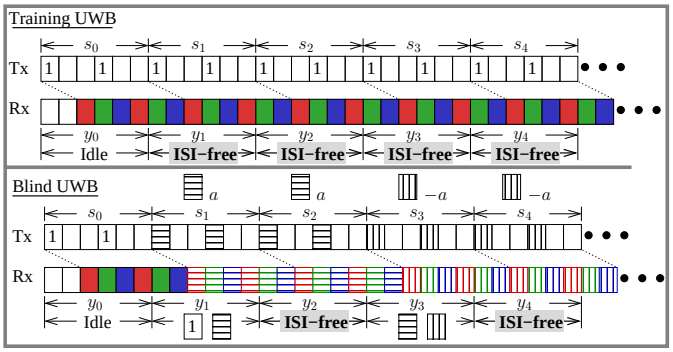

Fig. 4: Examples of circular convolution model formed from the inherent UWB symbol repetition.

the CP for the next training symbol, allowing all the received training symbols naturally follow the circular convolution model. Similarly, the blind UWB transmits repeated symbol patterns of (a,a,-a,-a), where the first symbol with "a" acts as CP for the next symbol, while the first symbol with "-a" acts as CP for the next symbol. Therefore, in both training-based and blind UWB sensing methods, a subset of symbols is naturally ISI-free, as depicted in Fig. 4. Fourier-Transform-based sensing can only be applied to these ISI-free symbols, without requiring additional resources for adding CP.

F. UWB FDE Sensing Relying on the Fourier Transform

Therefore, the following circular convolution model is formed for a subset of UWB symbols:

$$y_{n,m}=y(t)|_{t=nMT_c+mT_c}=\sum_{p=0}^{P-1}h_p s_{n,<m-l_p>_M}+v_{n,m}, \tag{16}$$

which is valid for $1\le n\le N_1$ for training-based UWB and $\{n=2i\}_{i=1}^{\frac{N}{2}}$ for blind UWB, while $<\cdot>_M$ denotes the modulo operation having the modulus of M. For these circular convolutions, the transmitted UWB symbols can be expressed in the frequency domain (FD) as follows:

$$\overline{s}_{n,\overline{m}}=\tfrac{1}{\sqrt{M}}\sum_{m=0}^{M-1}s_{n,m}\omega_M^{-m\overline{m}}=\tfrac{a_n}{\sqrt{M}}\sum_{m=0}^{M-1}\beta_m^{\text{Tx}}\omega_M^{-m\overline{m}}=a_n\overline{\beta}_{\overline{m}}^{\text{Tx}}, \tag{17}$$

where the user signature in FD is given by $\overline{\beta}_{\overline{m}}^{\text{Tx}}=\frac{1}{\sqrt{M}}\sum_{m=0}^{M-1}\beta_m^{\text{Tx}}\omega_M^{-m\overline{m}}$. With the aid of the FD representation of (17), the received signal in the time domain (TD) of (4) can be extended by:

$$y_{n,m}=\tfrac{a_n}{\sqrt{M}}\sum_{p=0}^{P-1}h_p\sum_{\overline{m}=0}^{M-1}\overline{\beta}_{\overline{m}}^{\text{Tx}}\omega_M^{(m-l_p)\overline{m}}+v_{n,m}. \tag{18}$$

Following this, the received signal in the FD can be obtained by applying the FFT as:

$$\overline{y}_{n,\overline{m}}=\tfrac{1}{\sqrt{M}}\sum_{m=0}^{M-1}y_{n,m}\omega_M^{-m\overline{m}}=a_n\overline{\beta}_{\overline{m}}^{\text{Tx}}\sum_{p=0}^{P-1}h_p\omega_M^{-l_p\overline{m}}+\overline{v}_{n,\overline{m}}, \tag{19}$$

where we have:

$$\sum_{m=0}^{M-1}\omega_M^{(m-l_p)(\overline{m}'-\overline{m})}=\begin{cases} M, & \text{if } \overline{m}'=\overline{m} \\ 0, & \text{otherwise} \end{cases}. \quad (20)$$

Therefore, the single-tap FDE harnessed for removing user-specific time-hopping signature is expressed as:

$$\overline{y}'_{n,\overline{m}}=\frac{\overline{y}_{n,\overline{m}}}{\overline{\beta}^{\text{Tx}}_{\overline{m}}}=a_n\sum_{p=0}^{P-1}h_p[\mathbf{a}_R(l_p)]_{\overline{m}}+\frac{\overline{v}_{n,\overline{m}}}{\overline{\beta}^{\text{Tx}}_{\overline{m}}}, \quad (21)$$

where the $\overline{m}$-th element in the FD steering vector of $\mathbf{a}_R(l_p)\in\mathcal{C}^{M\times 1}$ is given by $[\mathbf{a}_R(l_p)]_{\overline{m}}=\omega_M^{-l_p\overline{m}}$. We note that for UWB using OFDM radar principles, the conditions of $c_0\geq c_{G-1}$ and $M_G\geq l_{p,0}+1$ are no longer required. However, having user signatures that have low powers in the FD should be avoided, otherwise the noise will be amplified in (21). In our simulations, we avoid the user signatures associated with $\min_{\forall\overline{m}}|\overline{\beta}^{\text{Tx}}_{\overline{m}}|<\frac{1}{10M}\sum_{\overline{m}=0}^{M-1}|\overline{\beta}^{\text{Tx}}_{\overline{m}}|$.

Based on (21), the following Fourier-transform-based sensing property can be obtained:

$$\mathbf{IDFT}\left[\mathbf{a}_R(l_p)\right]=\frac{1}{\sqrt{M}}\sum_{\overline{m}=0}^{M-1}\omega_M^{-l_p\overline{m}}\omega_M^{\overline{m}\overline{l}}=\frac{1}{\sqrt{M}}\omega_M^{\overline{m}(l-l_p)}, \quad (22)$$

which has a peak of $\sqrt{M}$ at $\{l=l_p\}_{p=0}^{P-1}$, and zeros at other delay indices $\{l\neq l_p\}_{p=0}^{P-1}$ that may carry sidelobes, leading to the desired peak-sidelobe orthogonality. Based on the received signal model of (4), following (19) and (21), the IDFT is invoked as follows:

$$\widetilde{y}_{n,l}=\frac{1}{\sqrt{M}}\sum_{\overline{m}=0}^{M-1}\overline{y}'_{n,\overline{m}}\omega_M^{\overline{m}\overline{l}}=\frac{a_n}{\sqrt{M}}\sum_{p=0}^{P-1}h_p\sum_{\overline{m}=0}^{M-1}\omega_M^{\overline{m}(l-l_p)}+\widetilde{v}_{n,l}, \quad (23)$$

which has peaks at $\{l=l_p\}_{p=0}^{P-1}$ and sidelobes at $\{l\neq l_p\}_{p=0}^{P-1}$. The target l_0 is the LoS delay index corresponding to the earliest peak, i.e. $\hat{l}_0=\min\ \forall\{\hat{l}_p\}_{p=0}^{\hat{P}-1}$, where $\{\hat{l}_p\}_{p=0}^{\hat{P}-1}$ denote the set of delay indices of $\hat{P}$ peaks that are greater than a threshold $\mathcal{T}$. Therefore, for training-based UWB, the peaks are calculated based on N_1 training symbols:

$$\{\hat{l}_p\}_{p=0}^{\hat{P}-1}=\text{arg}_{\forall l=0,1,\cdots,M-1}\left|\frac{1}{N_1}\sum_{n=1}^{N_1}\widetilde{y}_{n,l}\right|^2>\mathcal{T}. \quad (24)$$

For blind UWB, the peaks are calculated based on the $\frac{N}{2}$ transmissions, which do not share the same pulse amplitude/phase:

$$\{\hat{l}_p\}_{p=0}^{\hat{P}-1}=\text{arg}_{\forall l=0,1,\cdots,M-1}\frac{2}{N}\sum_{i=1}^{\frac{N}{2}}|\widetilde{y}_{2i,l}|^2>\mathcal{T}. \quad (25)$$

As shown in (24) and (25), multiple targets represented by $\hat{P}$ sensing peaks $\{\hat{l}_p\}_{p=0}^{\hat{P}-1}$ can be detected by the proposed FDE method, whereas the conventional training-based, blind and LoS-based UWB MF sensing methods introduced in Secs III.B-D are limited to detecting only the single LoS target represented by $\hat{l}'_0$.

G. Data Detection for UWB Sensing Header

For training-based UWB, upon obtaining the synchronized $\hat{l}'_0$, data detection used for the UWB sensing header operating in the LRP mode can be performed as follows:

$$\begin{aligned}\hat{a}_n&=\text{arg}\min_{\forall a_n}\left|\sum_{m=\hat{l}'_0}^{M+\hat{l}'_0-1}y_{n,m}(\hat{\beta}^{\text{Rx}}_{m-l'_0})^*-a_n\sum_{m=\hat{l}'_0}^{M+\hat{l}'_0-1}|\hat{\beta}^{\text{Rx}}_{m-l'_0}|^2\right|^2\\&=\text{arg}\min_{\forall a_n}|z_n-a_n|^2,\end{aligned} \quad (26)$$

where the decision variable is given by $z_n=\left[\sum_{m=\hat{l}'_0}^{\hat{l}'_0+M-1}y_{n,m}(\hat{\beta}^{\text{Rx}}_{m-l'_0})^*\right]/\left(\sum_{m=\hat{l}'_0}^{\hat{l}'_0+M-1}|\hat{\beta}^{\text{Rx}}_{m-l'_0}|^2\right)$, and we have $N_1+1\leq n\leq N_1+N$.

Similar to the training-based UWB, the first transmission $\{y_{0,m}\}$ is left idle because it does not contain the same ISI pattern as the following symbols. Nonetheless, having obtained the synchronized $\hat{l}'_0$, this idle symbol can be used for obtaining the estimated aggregate receive-pulse template for blind UWB:

$$\hat{\beta}^{\text{Rx}}_{m-l'_0}=\begin{cases} y_{0,m}, & \text{for } \hat{l}'_0\leq m<M \\ y_{1,m}, & \text{for } 0\leq m<\hat{l}'_0 \end{cases}. \quad (27)$$

Following this, data detection can be performed for the blind UWB header in the same way as (26). For the LoS-based UWB header, the decision variable is $z_n=(\sum_{m=\hat{l}'_0}^{\hat{l}'_0+M-1}y_{n,m}\beta^{\text{Tx}}_{m-\hat{l}'_0})(\sum_{m=\hat{l}'_0}^{\hat{l}'_0+M-1}\hat{\beta}^{\text{Rx}}_{m-l'_0}\beta^{\text{Tx}}_{m-\hat{l}'_0})^*/|\sum_{m=\hat{l}'_0}^{\hat{l}'_0+M-1}\hat{\beta}^{\text{Rx}}_{m-l'_0}\beta^{\text{Tx}}_{m-\hat{l}'_0}|^2$.

IV. UWB Data Payload: How to Improve Data Rate?

In this section, the UWB payload model and the conventional MF template-based data detection are presented in Sec. IV-A and Sec. IV-B, respectively. The CIR estimation based on the first stage of FDE for UWB sensing is conceived in Sec. IV-C, which facilitates the second stage of FDE for PR-T data detection in Sec. IV-D. Finally, the achievable rates of the UWB payload are evaluated in Sec. IV-D.

A. UWB Payload Model in HRP Mode

Since generally a higher PRF is used for the UWB data payload operating in HRP mode, we denote the PRF and the number of chips per PRI by $\ddot{B}_G=B_S\ddot{G}$ and $\ddot{M}_G=\frac{M}{\ddot{G}}$, respectively, where $\ddot{G}$ refers to the number of pulses per symbol. The notations for the total number of chips per symbol M, symbol duration $T_S=\frac{1}{B_S}$, symbol rate B_S, chip duration $T_c=\frac{1}{B_c}$ and bandwidth B_c all remain the same. Based on (2), the payload data transmission is denoted by:

$$\begin{aligned}s_{n,m}&=\sqrt{\epsilon}\sum_{n=-\infty}^{\infty}a_n\sum_{g=0}^{\ddot{G}-1}\delta(m-g\ddot{M}_G-c_g-b_n\Delta)\\&=\sum_{n=-\infty}^{\infty}a_n\ddot{\beta}^{\text{Tx}}_{m-b_n\Delta},\end{aligned} \quad (28)$$

where the transmit-pulse template is given by $\ddot{\beta}^{\text{Tx}}_m=\sqrt{\epsilon}\sum_{g=0}^{\ddot{G}-1}\delta(m-g\ddot{M}_G-c_g)$. Similarly, based on (4), the received UWB payload symbols are modelled as:

$$\begin{aligned}y_{n,m}&=\sqrt{\epsilon}\sum_{n=-\infty}^{\infty}a_n\sum_{p=0}^{P-1}h_p\sum_{g=0}^{\ddot{G}-1}\delta(m-g\ddot{M}_G-c_g-l_p-b_n\Delta)\\&\quad+v_{n,m}=\sum_{n=-\infty}^{\infty}a_n\ddot{\beta}^{\text{Rx}}_{m-b_n\Delta-l_0}+v_{n,m},\end{aligned} \quad (29)$$

where the receive-pulse template is updated by $\ddot{\beta}^{\text{Rx}}_m=\sqrt{\epsilon}\sum_{p=0}^{P-1}h_p\sum_{g=0}^{\ddot{G}-1}\delta(m-g\ddot{M}_G-c_g-l_{p,0})$.

B. Conventional MF Template-Based Data Detection

Similarly to the data detection of Sec. III-G used for the UWB header, the UWB data payload can be detected based on the receive-pulse template. In order to update the template with a higher PRF, the CIRs are extracted from the UWB header receive-pulse template $\hat{\beta}^{\text{Rx}}_{m-l'_0}$ as follows:

$$\hat{h}_p=\frac{1}{\sqrt{\epsilon}G}\sum_{g=0}^{G-1}\hat{\beta}^{\text{Rx}}_{gM_G+c_g+p-l'_0},\ 0\leq p\leq\hat{P}, \quad (30)$$

where we may set $\hat{P}=\ddot{M}_G$, when the number of fading elements is unknown. Following this, the receive-pulse template for the payload data can be estimated by:

$$\hat{\ddot{\beta}}^{\text{Rx}}_{m-l'_0}=\sum_{p=0}^{\hat{P}-1}\sqrt{\epsilon}\hat{h}_p\delta(m-g\ddot{M}_G-c_g-p), \quad (31)$$

where we have $\hat{l}_p=\hat{l}_0+p$ and $\hat{l}_{0,p}=p$. We note that for the special case of $G=\ddot{G}$, where the PRF of the header and that of the payload are the same, we can directly use the same estimated template $\hat{\ddot{\beta}}^{\text{Rx}}_{m-l'_0}=\hat{\beta}^{\text{Rx}}_{m-l'_0}$. Following this, UWB payload data detection of PPM

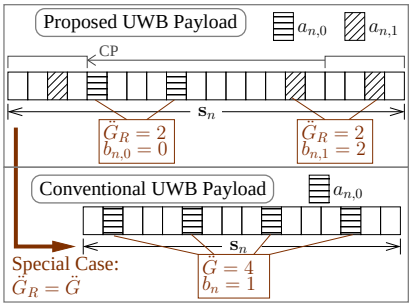

Fig. 5: Examples of the proposed PR-T scheme for UWB payload, where $M = 16$, $\ddot{G} = 4$, $\ddot{G}_R = 2$, $\ddot{M}_G = 4$ and $\{c_g = 0\}_{g=0}^{\ddot{G}-1}$.

can be performed for both the training-based and blind UWB schemes as $\{\hat{a}_n, \hat{b}_n\} = \arg\min_{\forall a_n, \forall b_n} \left| z_n^{b_n} - a_n \right|^2$, where the decision variable is given by $z_n^{b_n} = \left[\sum_{m=\hat{l}'_0}^{\hat{l}'_0+M-1} y_{n,m+b_n\Delta} (\hat{\bar{\beta}}^{\text{Rx}}_{m-l'_0})^*\right] / \left(\sum_{m=\hat{l}'_0}^{\hat{l}'_0+M-1} |\hat{\bar{\beta}}^{\text{Rx}}_{m-l'_0}|^2\right)$, while we have $n > N_1 + N$ and $n > 1 + N$ for the training and blind UWB schemes, respectively.

C. Channel Estimation Based on UWB FDE Sensing

Alternative to the CIRs estimated based on the receive-pulse template of Sec. IV-B, the proposed UWB FDE sensing method of Sec. III-F can directly provide the estimated CIRs. Based on (23) and (24), for the training-based UWB scheme, the CIRs estimated by UWB FDE sensing are given by:

$$\hat{h}_p = \frac{\sqrt{M}}{N_1} \sum_{n=1}^{N_1} \widetilde{y}_{n,\hat{l}_p}, \tag{32}$$

for $0 \le p \le \hat{P} - 1$. Similarly, based on (23) and (25), for the blind UWB scheme, the CIRs estimated by UWB FDE sensing are given by:

$$\hat{h}_p = \frac{2\sqrt{M}}{\hat{a}_{2i} N} \sum_{i=1}^{\frac{N}{2}} \widetilde{y}_{2i,l}, \tag{33}$$

for $0 \le p \le \hat{P} - 1$, where the UWB sensing data symbols $\hat{a}_{2i}$ are detected based on Sec. III-G. Following this, the estimated CIR taps $\{\hat{h}_p\}_{p=0}^{\hat{P}-1}$ and their delay indices $\{\hat{l}_p\}_{p=0}^{\hat{P}-1}$ obtained by UWB FDE sensing are utilized for performing UWB FDE data detection for the proposed PR-T in the next section.

D. Pulse Repetition Tradeoff (PR-T)

In order to follow the circular convolution model and facilitate FDE, in the absence of inherent symbol repetition in the UWB payload, concatenating a CP to the UWB payload becomes inevitable. However, since the LoS delay $\hat{l}_0$ has already been detected by UWB header sensing, the CP length only has to cover the synchronized delay spread $\{l_{p,0} = l_p - l_0\}_{p=0}^{P-1}$ instead of the full delays $\{l_p\}_{p=0}^{P-1}$. Since the ISI can be mitigated by FDE, the UWB pulse repetition within each symbol can be further reduced in order to achieve a higher throughput, without increasing the duty cycle.

Therefore, we propose a new PR-T scheme for the UWB payload, which is exemplified by Fig. 5. Explicitly, the UWB data payload symbol is constituted by $M + \ddot{M}_G$ chips, where the last PRI is copied and placed at the beginning of an UWB symbol as CP. During a symbol transmission, a pulse is repeated $\ddot{G}_R$ times instead of $\ddot{G}$ times, where $\ddot{G}/\ddot{G}_R$ different pulses are modulated. The range is $1 \le \ddot{G}_R \le \ddot{G}$. Therefore, the PR-T scheme proposed for UWB payload modulation is formulated as (34), where the impulse index is given by $g = r\ddot{G}_R + g_r$. As a result, the repetition gain is reduced from $\ddot{G}$ to $\ddot{G}_R$, but the throughput is increased from $\log_2 \mathcal{A} + \log_2 \mathcal{B}$ to $(\log_2 \mathcal{A} + \log_2 \mathcal{B}) \frac{\ddot{G}}{\ddot{G}_R} \frac{\ddot{G}}{\ddot{G}+1}$, where the cost of CP is accounted for by the factor $\frac{\ddot{G}}{\ddot{G}+1}$, while $\mathcal{A}$ and $\mathcal{B}$ refer to the cardinalities of pulse amplitude/phase and positions, respectively. The constant delay in (34) is given by $\Delta = \lfloor \frac{c_0 - c_{G-1}}{\mathcal{B}/2} \rfloor$. Moreover, the special cases of (34) associated with $\ddot{G}_R = \ddot{G}$ and $\ddot{G}_R = 1$ correspond to the PPM of (28) and index modulation, respectively.

Thanks to the CP in (34), the linear convolution model of (4) becomes the following circular convolution model:

$$y_{n,m} = y(t)|_{t=n(M+\ddot{M}_G)T_c + \ddot{M}_G + mT_c} = \sum_{p=0}^{P-1} h_p s_{n,<m-l_p>_M} + v_{n,m}, \tag{36}$$

which is valid during the UWB payload transmission of $n > N_1 + N + 1$ for training-based UWB and $n > N + 1$ for blind UWB. Therefore, the single-tap FDE for data detection can be expressed as:

$$\hat{\bar{z}}_{n,\overline{m}} = \overline{y}_{n,\overline{m}} / \hat{\bar{h}}_{n,\overline{m}}, \quad 0 \le \overline{m} \le M - 1 \tag{37}$$

where the FD received signal is obtained by applying the DFT to (36) as $\overline{y}_{n,\overline{m}} = \frac{1}{\sqrt{M}} \sum_{m=0}^{M-1} y_{n,m} \omega_M^{-m\overline{m}} = \overline{h}_{n,\overline{m}} \overline{s}_{n,\overline{m}} + \overline{v}_{n,\overline{m}}$, while the estimated channel frequency responses (CFRs) are obtained by $\hat{\bar{h}}_{n,\overline{m}} = \sum_{p=0}^{\hat{P}-1} \hat{h}_p \omega_M^{-\overline{m}\hat{l}_{p,0}}$. The CIR taps $\{\hat{h}_p\}_{p=0}^{\hat{P}-1}$ and synchronized delay spreads $\{\hat{l}_{p,0}\}_{p=0}^{\hat{P}-1}$ are obtained from the UWB sensing header.

Following this, the ML detection of the amplitude/phase and position of the r-th pulse can be performed in the TD as:

$$(\hat{a}_{n,r}, \hat{b}_{n,r}) = \arg \min_{\forall a_{n,r}, \forall b_{n,r}} d^2(a_{n,r}, b_{n,r}), \tag{38}$$

where the decision variable is given by $d^2(a_{n,r}, b_{n,r}) = |\sum_{m=r\ddot{G}_R\ddot{M}_G}^{r\ddot{G}_R\ddot{M}_G + \ddot{G}_R\ddot{M}_G - 1} z_{n,m} - a_{n,r} \sum_{g_r=0}^{\ddot{G}_R-1} \delta\left(m - g\ddot{M}_G - < c_g + b_{n,r}\Delta >_{\ddot{M}_G}\right)|^2$. The full-search based ML detection has the complexity order of $\mathcal{O}(\mathcal{AB})$. To mitigate this complexity, energy detection can be invoked for pulse position detection first according to $\hat{b}_{n,r} = \arg \max_{\forall b_{n,r}} \left| \sum_{\forall m = g\ddot{M}_G + < c_g + b_{n,r}\Delta >_{\ddot{M}_G}} z_{n,m} \right|^2$, which leads to a performance loss since the pulse amplitude/phase is not considered in pulse position detection. As a remedy, the reduced-complexity ML detection conceived for index modulation in [43] can be invoked to implement (38) by the following three steps of (i) demodulation for each index, (ii) index detection and (iii) final decision:

$$\begin{aligned} &\hat{a}_{n,r}(b_{n,r}) = \mathbb{M}^{-1}(\textstyle\sum_{\forall m = g\ddot{M}_G + < c_g + b_{n,r}\Delta >_{\ddot{M}_G}} z_{n,m}), \\ &\hat{b}_{n,r} = \arg \max_{\forall b_{n,r}} d^2\left(\hat{a}_{n,r}(b_{n,r}), b_{n,r}\right), \\ &\hat{a}_{n,r} = \hat{a}_{n,r}(\hat{b}_{n,r}). \end{aligned} \tag{39}$$

Note that the single-stream demodulation $\mathbb{M}^{-1}(z)$ can round the amplitude/phase of the decision variable z to the nearest constellation [47]. For $\mathcal{A}$-PSK, the optimal phase index can be detected as $\lfloor \frac{\mathcal{A}}{2\pi} \angle z \rceil$. For $\mathcal{A}$-PAM, the optimal amplitude index can be detected as $\max[\min(\lfloor (\mathcal{A} - \sqrt{\eta} z - 1)/2 \rceil, \mathcal{A} - 1), 0]$, where $\eta = \sum_{\iota=0}^{\mathcal{A}/2-1} (\mathcal{A} - 2\iota + 1)^2 / (\mathcal{A}/2)$ normalizes the PAM symbol power. For $\mathcal{A}$-QAM, the real and imaginary parts of z are demodulated as $\sqrt{\mathcal{A}}$-QAM, where the constellation normalization factor is given by $\eta = \sum_{\iota=0}^{\sqrt{\mathcal{A}}/2-1} (\mathcal{A} - 2\iota + 1)^2 / (\sqrt{\mathcal{A}}/4)$.

$$s_{n,m} = s(t)|_{t=n(M+\ddot{M}_G)T_c+\ddot{M}_G+mT_c} = \begin{cases} s_{n,M+m}, & -\ddot{M}_G \le m \le -1 \\ \sqrt{\epsilon}\sum_{r=0}^{\ddot{G}/\ddot{G}_R-1} a_{n,r} \sum_{g_r=0}^{\ddot{G}_R-1} \delta\left(m - g\ddot{M}_G - < c_g + b_{n,r}\Delta >_{\ddot{M}_G}\right), & 0 \le m \le M \end{cases}, \tag{34}$$

$$p(\{z_{n,m}\}_{m=r\ddot{G}_R\ddot{M}_G}^{r\ddot{G}_R\ddot{M}_G+\ddot{G}_R\ddot{M}_G-1}|a^\imath, b^\jmath) = \frac{1}{\pi N_0'} \exp\left(-\frac{\left|\sum_{m=r\ddot{G}_R\ddot{M}_G}^{r\ddot{G}_R\ddot{M}_G+\ddot{G}_R\ddot{M}_G-1} z_{n,m} - a^\imath \sum_{g_r=0}^{\ddot{G}_R-1} \delta\left(m - g\ddot{M}_G - < c_g + b^\jmath\Delta >_{\ddot{M}_G}\right)\right|^2}{N_0'}\right). \tag{35}$$

E. Achievable Rates with Estimated CIRs

Based on the conventional UWB MF template-based payload data detection in Sec. IV-B, the achievable rate with CIRs estimated by UWB MF is given by [14], [47], [48]:

$$\mathcal{C} = \frac{B_c}{M} E\left[\log_2 \frac{\mathcal{AB}p(\{y_{n,m+b_n\Delta}\}_{m=\hat{l}_0'}^{\hat{l}_0'+M-1}|a^\imath, b^\jmath)}{\sum_{\imath'=0}^{\mathcal{A}-1}\sum_{\jmath'=0}^{\mathcal{B}-1} p(\{y_{n,m+b_n\Delta}\}_{m=\hat{l}_0'}^{\hat{l}_0'+M-1}|a^{\imath'}, b^{\jmath'})}|a^\imath, b^\jmath\right], \tag{40}$$

where equiprobable symbols are assumed, i.e. we have $\{p(a^\imath) = \frac{1}{\mathcal{A}}\}_{\imath=0}^{\mathcal{A}-1}$ and $\{p(b^\jmath) = \frac{1}{\mathcal{B}}\}_{\jmath=0}^{\mathcal{B}-1}$, and the conditional probability is given by:

$$p(\{y_{n,m+b_n\Delta}\}_{m=\hat{l}_0'}^{\hat{l}_0'+M-1}|a^\imath, b^\jmath) = \frac{1}{\pi(\sum_{m=\hat{l}_0'}^{\hat{l}_0'+M-1}|\hat{\beta}_{m-l_0'}^{\mathrm{Rx}}|^2)N_0} \times \exp\left(-\frac{\left|\sum_{m=\hat{l}_0'}^{\hat{l}_0'+M-1} y_{n,m+b^\jmath\Delta}(\hat{\beta}_{m-l_0'}^{\mathrm{Rx}})^* - a^\imath \sum_{m=\hat{l}_0'}^{\hat{l}_0'+M-1}|\hat{\beta}_{m-l_0'}^{\mathrm{Rx}}|^2\right|^2}{(\sum_{m=\hat{l}_0'}^{\hat{l}_0'+M-1}|\hat{\beta}_{m-l_0'}^{\mathrm{Rx}}|^2)N_0}\right). \tag{41}$$

Based on the proposed UWB FDE payload data detection of (38), the achievable rate with CIRs estimated by UWB FDE is given by:

$$\mathcal{C} = \frac{B_c\ddot{G}}{M(\ddot{G}+1)} \sum_{r=0}^{\ddot{G}/\ddot{G}_R-1} E\left[\log_2 \frac{\mathcal{AB}p(\{z_{n,m}\}_{m=r\ddot{G}_R\ddot{M}_G}^{r\ddot{G}_R\ddot{M}_G+\ddot{G}_R\ddot{M}_G-1}|a^\imath, b^\jmath)}{\sum_{\imath'=0}^{\mathcal{A}-1}\sum_{\jmath'=0}^{\mathcal{B}-1} p(\{z_{n,m}\}_{m=r\ddot{G}_R\ddot{M}_G}^{r\ddot{G}_R\ddot{M}_G+\ddot{G}_R\ddot{M}_G-1}|a^{\imath'}, b^{\jmath'})}|a^\imath, b^\jmath\right], \tag{42}$$

where the CP overhead is normalized by $\frac{\ddot{G}}{(\ddot{G}+1)}$, while the conditional probability is given by (35). The FDE noise power is formulated as $N_0' = \frac{MN_0}{\sum_{\overline{m}=0}^{M-1}|\hat{\bar{h}}_{n,\overline{m}}|^2}$.

V. Performance Results

In this section, we consider an UWB system having a bandwidth of $B_c = 512$MHz and a symbol rate of $B_S = 1$MHz, where there are $M = 512$ chips within the duration of a UWB symbol. The carrier frequency is set to $f_c = 7$GHz. The number of pulses per symbols is configured as $G = 16$ and $G = 64$ for the LPR and HPR modes, respectively. The remaining UWB simulation parameters, including the Ricean K-factor, the number of training symbols N_1, the number of data-carrying UWB sensing symbols N, the UWB FDE sensing detection threshold $\mathcal{T}$, the PAM/PSK/QAM constellations and the distance between the transmitter and receiver are investigated individually in the following subsections.

A. UWB Sensing Experiment Highlighting an Open Problem

Our demonstration of conventional UWB sensing is presented in Fig. 6, using Qorvo's DW3000 module [46]. The user wears a tag and walks along a rectangular track, with a Kalman filter employed to smoothen the trajectory of the user's movement. Firstly, when the user places the tag on top of their head, which creates a strong LoS condition to three anchors, the UWB measurements achieve centimeter-level accuracy, as demonstrated by Fig. 6a. However, when the user wears the tag on their back, as depicted in Fig. 6c, this creates a LoS blockage to at least one anchor at one time. As a result, some of the UWB measurements suffer from severely degraded sensing accuracy that can be on the order of several meters, as demonstrated by Fig. 6b. The degraded measurements guide the Kalman filter completely off-track. To address this issue, we opt for ignoring measurements that have negative Ricean K-factors, which can be inferred from the ratio between first path power and the total received signal power in DW3000 measurements [46]. Fig. 6d shows significantly improved measurements and tracking results using this approach.

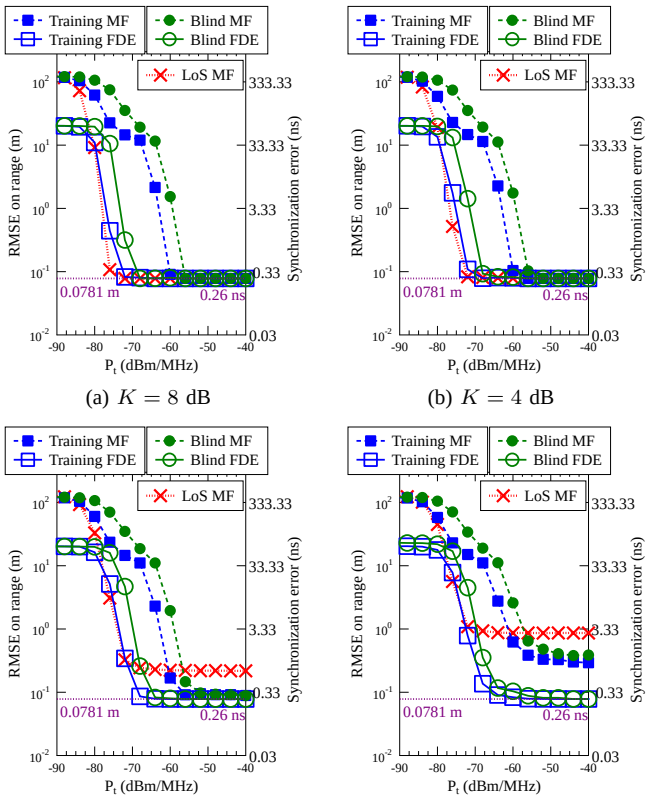

(a) $K = 8$ dB (b) $K = 4$ dB

(c) $K = 0$ dB (d) $K = -4$ dB

Fig. 7: Effect of K on UWB header: RMSE on range for UWB MF and FDE sensing methods, where we have $M = 512$, $G = 16$, $B_c = 512$MHz, $P = 8$ and $d = 20$ m, while 2PAM is used.

Although a Kalman filter can moderate unreliable measurements for moving users, a stationary user – such as a patient, an elderly person or a IoT device may experience a blocked LoS view to an anchor for a long time, during which no reliable measurements with non-negative Ricean K-factors can be obtained. Therefore, in the remainder of this paper, we present simulation results demonstrating the theoretical improvements for UWB ISAC transceiver, particularly in NLoS scenarios.

B. Effect of Ricean K-factor on UWB Sensing

Fig. 7 illustrates the UWB MF and FDE sensing performance in terms of its root mean squared error (RMSE) for range estimation. Explicitly, the RMSE of range is given by

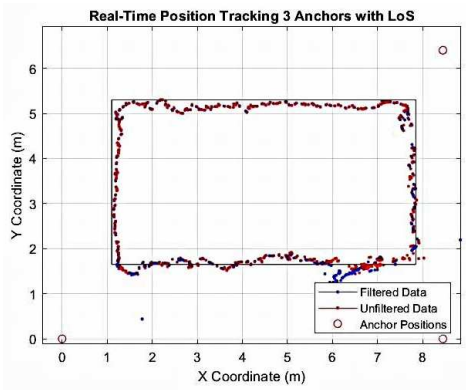

(a) LoS

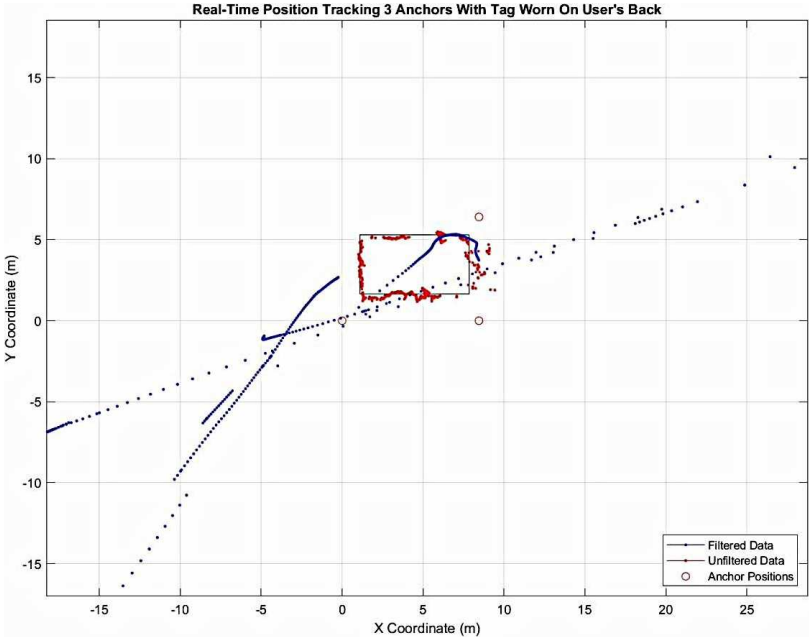

(b) NLoS

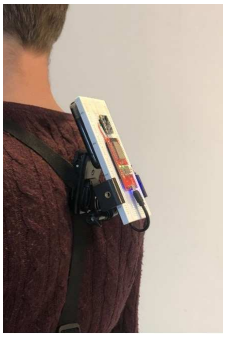

(c) Tag NLoS

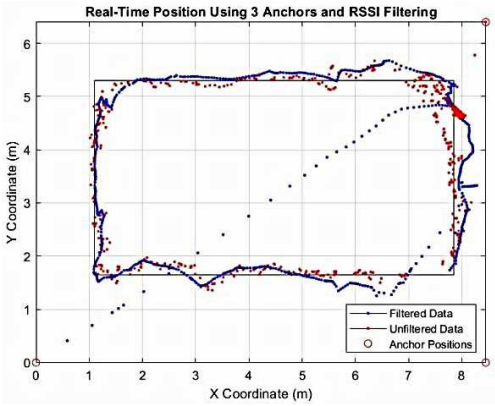

(d) Additional NLoS Filtering

Fig. 6: Effect of NLoS in UWB experiment using Qorvo's DW3000 module [46], where red-colored "unfiltered data" and blue-colored "filtered data" refer to the UWB measurements without and with Kalman filtering, respectively. (a) LoS scenario, where the user places the tag on top of their head; (b) NLoS scenario, where the user wears the tag on their back; (c) Location of the tag in NLoS scenario; (d) Additional NLoS filtering, where measurements with negative Ricean K-factors are ignored.

$|d - \hat{l}_0 c/B_c|$, where $\hat{l}_0$ refers to the UWB estimated delay. Since the UWB estimated delay $\hat{l}_0$ is also used for time-stamp synchronization between the tag and anchor, the synchronization error is calculated as $|d/c - \hat{l}_0/B_c|$. For a tag-anchor distance of $d = 20$ m exemplified by Fig. 7, the UWB sensing lower bound is determined by the residual fractional delay index $|d \cdot B_c/c - \lfloor d \cdot B_c/c \rceil| \approx 0.133$, which corresponds to $0.133c/B_c = 0.0781$ m and $0.133/B_c = 0.26$ ns for ranging RMSE and synchronization error, respectively. As shown in Fig. 7a), all UWB sensing methods converge to the lower bound. Additionally, Figs. 7a)-d) demonstrate that the UWB MF sensing performance degrades severely as the Ricean K-factor decreases. By contrast, the proposed UWB FDE sensing methods are still capable of converging to the centimeter-level ranging lower bound and nanosecond-level synchronization error lower bound, even at a low Ricean K-factor of -4 dB.

The sensing performance results shown in Fig. 7 are further verified by Fig. 8, where the sensing amplitudes are presented in an ideal noise-free scenario. Fig. 8a) and Fig. 8c) representing training-based and blind UWB MF schemes demonstrate that the sidelobes in UWB MF sensing are never zero, not even under noise-free conditions, and the peak-to-sidelobe power ratio is significantly reduced, as the Ricean K-factor decreases. By contrast, Fig. 8b) and Fig. 8d) recorded for training-based and blind UWB FDE schemes show that UWB FDE sensing achieves orthogonality between the peaks to sidelobes, where the sidelobes are zero in noise-free conditions, while non-zero peaks represent CIR taps reflected from multiple targets. As the Ricean K-factor decreases from 8 dB to -4 dB, the peak amplitudes of UWB FDE sensing are reduced. However, the propagation delay can still be accurately detected as the time-of-arrival of the first peak without interferences from sidelobes, as shown in Fig. 8b) and Fig. 8d). As discussed in Sec. III-E, MF-based UWB sensing can only detect the time-of-arrival of a single target, as shown in Fig. 8a) and Fig. 8c), since the UWB MF receiver is required to accumulate multipath powers across all repeated pulses. By contrast, the UWB FDE sensing proposed in Sec. III-F decouples the multipath components and thus facilitates multi-target sensing, as illustrated in Fig. 8b) and Fig. 8d). Fig. 9 further confirms

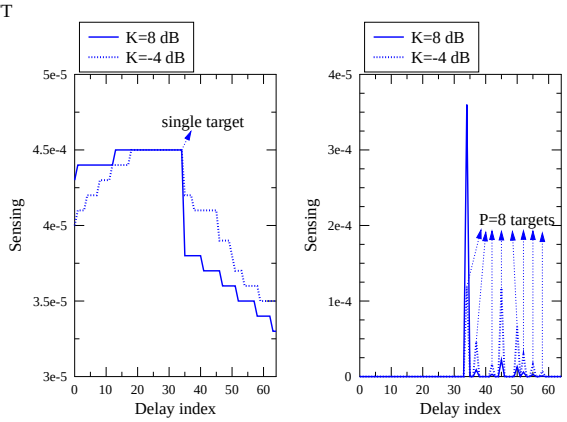

(a) Training, MF (b) Training, FDE

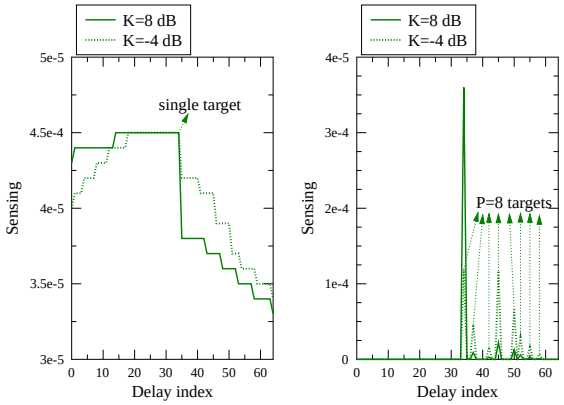

(c) Blind, MF (d) Blind, FDE

Fig. 8: Effect of K on UWB header: Training-based and blind UWB using MF and FDE sensing amplitudes in noise-free condition, where we have $M = 512$, $G = 16$, $B_c = 512$MHz, $P = 8$, $d = 20$ m and $P_t = -40$dBm/Hz, while 2PAM is used.

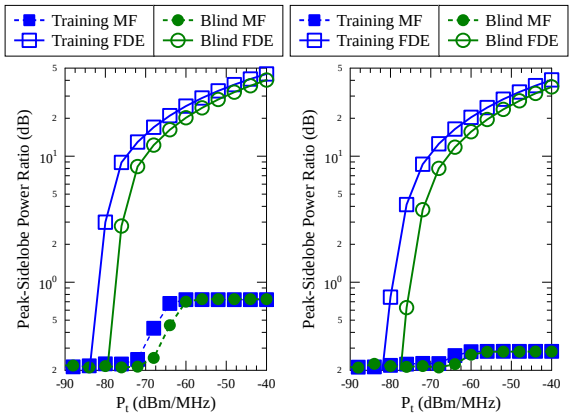

(a) $K = 8$ dB (b) $K = -4$ dB

Fig. 9: Effect of K on UWB header: Peak-to-sidelobe power ratios of UWB MF and FDE sensing methods, where we have $M = 512$, $G = 16$, $B_c = 512$MHz, $P = 8$ and $d = 20$ m, while 2PAM is used.

that the proposed FDE sensing substantially improves the peak-to-sidelobe ratios of the conventional MF sensing for both training-based and blind UWB systems.

C. Effect of Ricean K-factor on UWB Data Detection

Fig. 10 portrays the effect of Ricean K-factor on the BER of UWB detection, where UWB MF and FDE sensing methods are used for synchronization and CIR estimation. As shown in Fig. 10, both the training-based and blind UWB FDE sensing methods outperform their MF counterparts. Figs. 10a) and b) further demonstrate that the LoS-based method achieves good

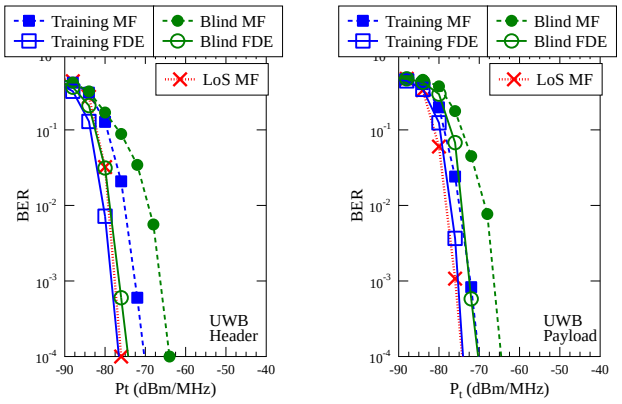

(a) Header,$K = 8$ dB (b) Payload,$K = 8$ dB

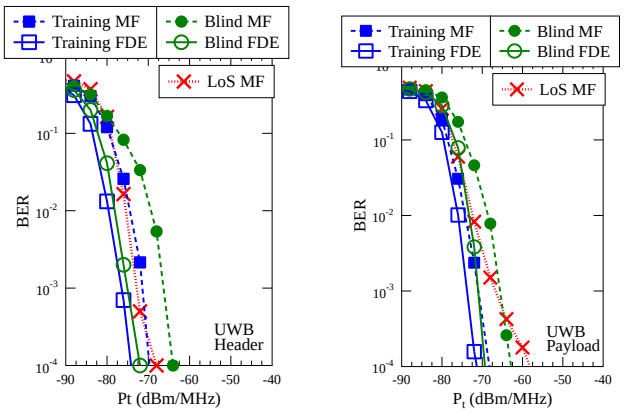

(c) Header,$K = -4$ dB (d) Payload,$K = -4$ dB

Fig. 10: Effect of K on UWB data detection: BER of UWB header using 2PAM and UWB data payload using 2PAM and 2PPM. The parameters are $M = 512$, $G = \ddot{G} = \ddot{G}_R = 16$, $B_c = 512$MHz, $P = 8$ and $d = 20$ m.

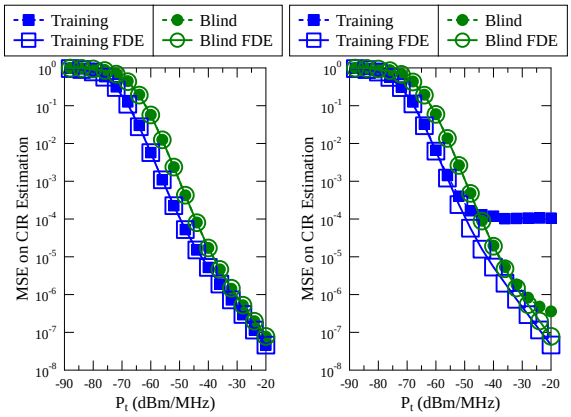

(a) $K = 8$ dB (b) $K = -4$ dB

Fig. 11: Effect of K on UWB data detection: Channel Estimation Errors of UWB MF and FDE schemes, where we have $M = 512$, $G = 16$, $B_c = 512$MHz, $P = 8$ and $d = 20$ m, while 2PAM is used.

performance at a high Ricean K-factor of 8 dB, which is a benefit of its advantageous synchronization capability in LoS scenarios, as presented in Fig. 7a). The LoS-based UWB MF sensing utilizes the user-specific time-hopping sequence as its correlation template, which has ideal zero-valued off-peak auto-correlation functions. However, Figs. 10c) and d) show that the LoS-based UWB scheme exhibits degraded BER performance at a low Ricean K-factor of -4 dB, due to its severely impaired synchronization performance, as depicted in Fig. 7d). Furthermore, as expected, Fig. 10 evidences that the proposed training-based and blind FDE methods achieve better performance than their conventional MF counterparts.

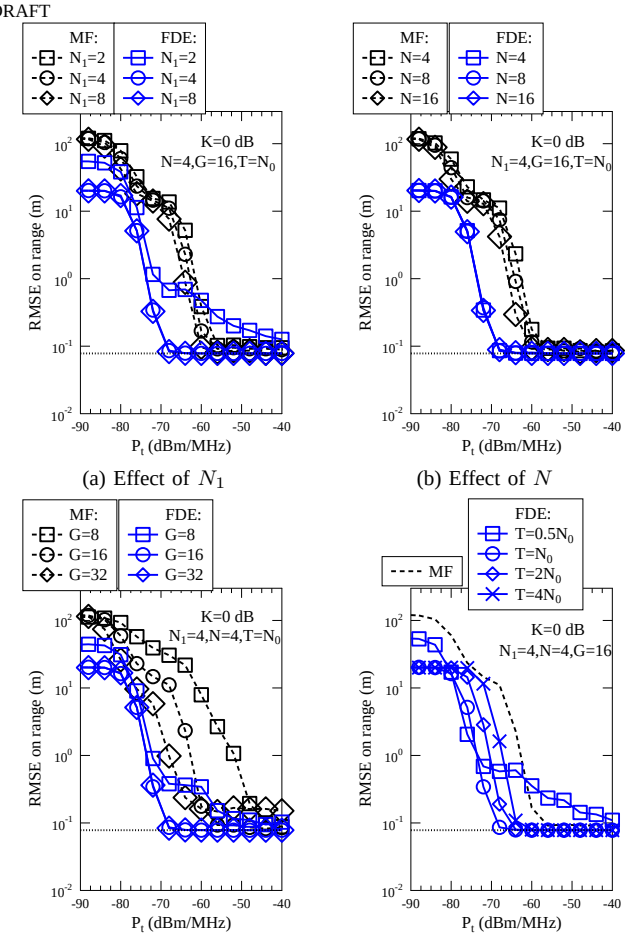

Fig. 12: Impact of UWB header parameters: RMSE on range for training-based UWB MF and FDE sensing methods, where we have $M = 512$, $B_c = 512$MHz, $P = 8$ and $d = 20$ m, while 2PAM is used.

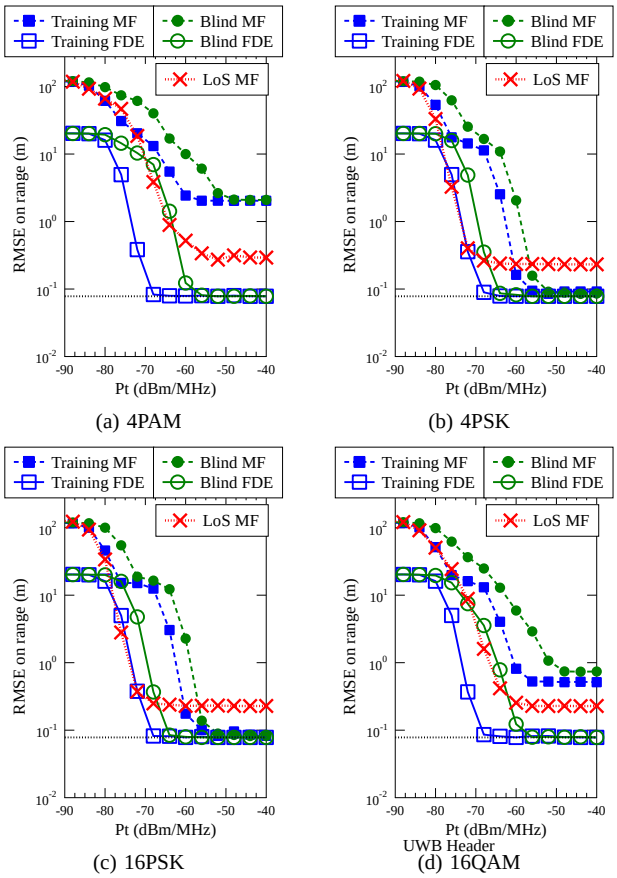

Fig. 13: Effect of UWB header modulation: RMSE on range for UWB MF and FDE sensing methods for UWB header, where we have $M = 512$, $G = 16$, $B_c = 512$MHz, $K = 0$dB, $P = 8$ and $d = 20$ m, while 2PAM/4PAM/4PSK/16PSK/16QAM are used.

To elaborate, the improved BERs achieved by FDE for UWB data detection in Fig. 10 result from the enhanced synchronization and CIR estimation provided by the first-stage of FDE for UWB sensing, as demonstrated in Fig. 7 and Fig. 11, respectively. As shown in Fig. 11, the CIRs estimated by training-based and blind UWB MF sensing exhibit error floors when the Ricean K factor is reduced to $K = -4$ dB. Similarly, Fig. 7 shows that both training-based and blind UWB MF sensing fail to converge to the synchronization lower bound at $K = -4$ dB. By contrast, the proposed UWB FDE improves synchronization and channel estimation for UWB data detection, particularly at a low Ricean K-factor of -4 dB, as shown in Fig. 7 and Fig. 11, respectively.

D. Impact of UWB Header Parameters

Fig. 12 investigates the impact of UWB header paramters, where training-based UWB MF and FDE sensing methods are invoked. Firstly, Fig. 12a) demonstrates that the performance of both MF and FDE improves, as the number of training symbols N_1 used for estimating the "clean template" in (10) increases. The improvement in FDE sensing becomes negligible, when $N_1 \geq 4$. Secondly, Fig. 12b) indicates that the MF sensing performance improves, as the number of data-carrying UWB sensing symbols N employed for estimating the delay in (11) increases. However, the FDE sensing performance is less affected by changes in N. Thirdly, Fig. 12c) shows that both the MF and FDE sensing performance improves, as the number of pulses per UWB symbol G is increased for enhancing the pulse repetition gain. Nonetheless, the improvement in FDE sensing becomes negligible, when $G \geq 16$. Finally, Fig. 12d) demonstrates that $\mathcal{T} = N_0$ is the preferred threhold for the training-based UWB FDE sensing of (24), where a smaller threshold, such as $\mathcal{T} = 0.5N_0$, is buried under the noise floor, while a larger $\mathcal{T} \geq 2N_0$ leads to late convergence.

E. Effect of UWB Header Modulation

The data-carrying PAM/PSK/QAM modulations, inherently repeated in UWB pulses, do not interfere with the proposed UWB FDE sensing operations of Sec. III-F. Consequently, high-order PAM/PSK/QAM modulation can be employed by the proposed UWB FDE sensing, as confirmed by Fig. 13. By contrast, the conventional UWB MF sensing methods suffer from degraded performance under the same conditions. The correlation-based MF sensing methods, including LoS-based, training-based and blind methods, perform particularly worse, when 4PAM and 16QAM are used to modulate UWB pulse amplitude/phase, as evidenced by Figs. 13a) and d).

F. Effect of Distance Between Transmitter and Receiver

Figs. 14a)-d) demonstrate that as the distance between the transmitter and receiver increases, the performance of both UWB MF and FDE sensing methods generally degrades. However, the proposed training-based and blind UWB FDE sensing methods consistently outperform their MF counterparts, as evidenced by Figs. 14a)-d), where the transmit

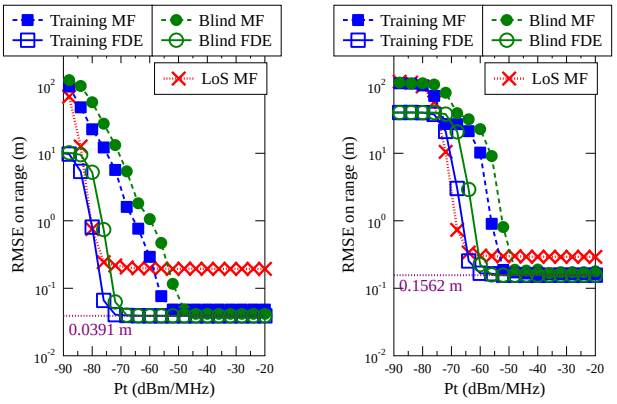

(a) d=10 m (b) d=40 m

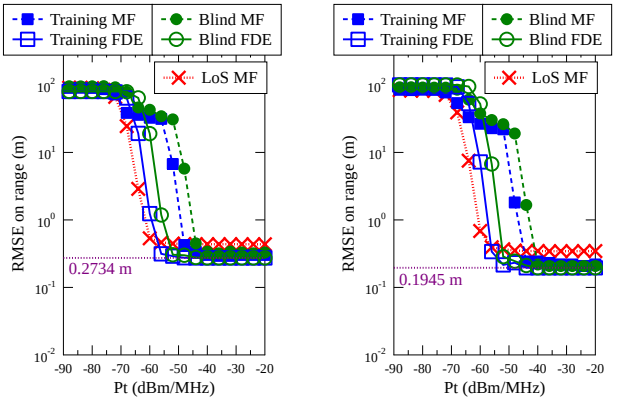

(c) d=80 m (d) d=100 m

Fig. 14: Effect of distance: RMSE on range for UWB MF and FDE sensing methods invoked for estimating different distances between transmitter and receiver, where we have $M = 512$, $G = 16$, $B_c = 512$MHz, $K = 0$dB and $P = 8$ for $d = \{10, 40, 80, 100\}$ m, while 2PAM is used.

powers P_t required for UWB FDE sensing methods to achieve centimeter-level accuracy are always below the UWB power mask of -40dBm/Hz.

G. Achievable Rates of PR-T for UWB Payload

The achievable rates evaluated in Sec. IV-E for UWB ISAC schemes are portrayed in Fig. 15a). The proposed two-tier FDE scheme, in which the first FDE removes the user-specific time-hopping sequence for sensing and the second FDE eliminates the effect of CIRs for data detection, outperforms conventional UWB MF ISAC with the same pulse repetition gain of $\ddot{G}_R = 64$, as shown in Fig. 15a). Furthermore, the proposed PR-T scheme achieves increased data rates of 7.875Mbps, 31.5Mbps and 126Mbps, at the cost of reduced pulse repetition gains of $\ddot{G}_R = 16$, $\ddot{G}_R = 4$ and $\ddot{G}_R = 1$, respectively. In these cases, the schemes having lower $\ddot{G}_R$ reach their data rate upper bound at higher P_t. Nonetheless, Fig. 15b) demonstrates that after normalizing P_t with respect to throughput, the PR-T schemes associated with higher throughput but lower $\ddot{G}_R$ exhibit better performance at both low and high normalized powers P_t per bit.

VI. Conclusions

A novel two-tier FDE scheme was conceived for UWB ISAC. The first single-tap FDE removes the user signature from the received UWB header for sensing, while the second single-tap FDE equalizes the CIRs in the received UWB

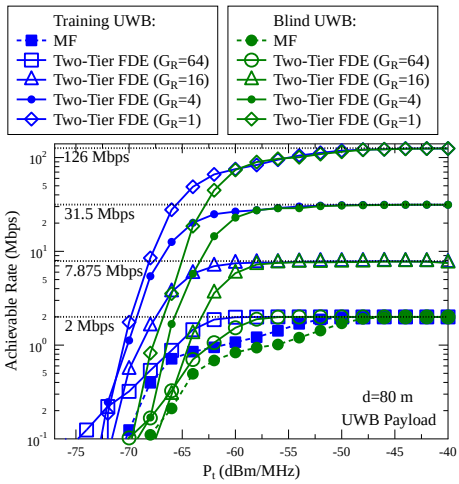

(a) d=80 m, P_t

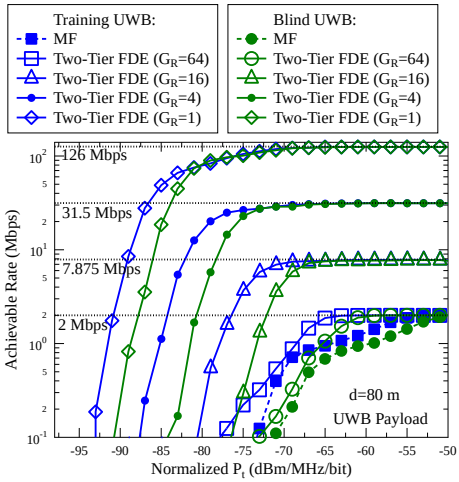

(b) d=80 m, Normalized P_t per bit

Fig. 15: PR-T for UWB Payload: Achievable rates of PR-T for UWB payload, where the two-tier FDE is deployed for UWB sensing and data detection. The parameters are $M = 512$, $G = 16$, $\ddot{G} = 64$, $B_c = 512$MHz, $K = 0$dB and $P = 8$ for $d = 80$ m.

payload for data detection. The CP overhead is eliminated for the UWB header by exploiting the inherent training/blind-based UWB symbol repetition patterns. In the UWB payload, the CP overhead is designed to be inversely proportional to the number of pulses per UWB symbol. The second stage of UWB FDE data detection directly utilizes the CIRs estimated by the first stage of UWB FDE sensing. This facilitates a novel PR-T scheme that allows for flexible trade-offs between throughput and pulse repetition gain. Our simulation results demonstrate that the proposed UWB FDE sensing achieves centimeter-level accuracy even at a low Ricean K-factor of -4 dB. Additionally, the FDE-aided UWB PR-T payload achieves a doubled data rate, when the pulse repetition gain is reduced by half.

References

[1] Ericsson, "6G-connecting a cyber-physical world," *[Online]. Available: https://www.ericsson.com/4927de/assets/ local/reports-papers/white-papers/6g-connecting-a-cyber-physical-world.pdf.*

[2] Huawei, "6G: The next horizon," *[Online]. Available: https://www-file.huawei.com/-/media/corp2020/pdf/tech-insights/1/6g-white-paper-en.pdf.*

[3] Intel, "Next-generation Wi-Fi: Wi-Fi 7 and beyond," *[Online]. Available: https://www.intel.com/content/dam/www/public/us/en/documents/pdf/wi-fi-7-and-beyond.pdf.*

[4] 3GPP Technical Specification 22.837, "Study on integrated sensing and communication," *[Online]. Available: http://www.3gpp.org/ftp//Specs/archive/22_series/22.837/.*

[5] 3GPP Technical Report 21.916, "Summary of Rel-16 work items," *[Online]. Available: http://www.3gpp.org/release-16*.

[6] D. Coppens, A. Shahid, S. Lemey, B. Van, C. Marshall, and E. D. Poorter, "An overview of UWB standards and organizations (ieee 802.15.4, fira, apple): Interoperability aspects and future research directions," *IEEE Access*, vol. 10, pp. 70219–70241, 2022.

[7] F. Zafari, A. Gkelias, and K. K. Leung, "A survey of indoor localization systems and technologies," *IEEE Commun. Surveys Tut.*, vol. 21, no. 3, pp. 2568–2599, 2019.

[8] M. Win and R. Scholtz, "Impulse radio: how it works," *IEEE Commun. Lett.*, vol. 2, no. 2, pp. 36–38, 1998.

[9] S. Gezici, T. Zhi, G. Giannakis, H. Kobayashi, A. Molisch, H. Poor, and Z. Sahinoglu, "Localization via ultra-wideband radios: a look at positioning aspects for future sensor networks," *IEEE Signal Process. Mag.*, vol. 22, no. 4, pp. 70–84, 2005.

[10] M. Hussain, "Ultra-wideband impulse radar - overview of the principles," *IEEE Aerosp. Electron. Syst. Mag.*, vol. 13, no. 9, pp. 9–14, 1998.

[11] L. Yang and G.B.Giannakis, "Ultra-wideband communications: an idea whose time has come," *IEEE Signal Process. Mag.*, vol. 21, no. 6, pp. 26–54, 2004.

[12] H. Sheng and A. M. Haimovich, "Impact of channel estimation on ultra-wideband system design," *IEEE J. Sel. Topics Signal Process.*, vol. 1, no. 3, pp. 498–507, 2007.

[13] V. Lottici, A. D'Andrea, and U. Mengali, "Channel estimation for ultra-wideband communications," *IEEE J. Sel. Areas Commun.*, vol. 20, no. 9, pp. 1638–1645, 2002.

[14] L. Hanzo, O. Alamri, M. El-Hajjar, and N. Wu, *Near-Capacity Multi-Functional MIMO Systems: Sphere-Packing, Iterative Detection and Cooperation*. John Wiley & Sons, May 2009.

[15] C. Xu, L. Xiang, J. An, C. Dong, S. Sugiura, R. G. Maunder, L.-L. Yang, and L. Hanzo, "OTFS-aided RIS-assisted SAGIN systems outperform their OFDM counterparts in doubly selective high-doppler scenarios," *IEEE Internet Things J.*, vol. 10, no. 1, pp. 682–703, 2023.

[16] C. Xu, L. Xiang, S. Sugiura, R. G. Maunder, L.-L. Yang, D. Niyato, G. Y. Li, R. Schober, and L. Hanzo, "Noncoherent orthogonal time frequency space modulation," *IEEE Trans. Wireless Commun. (accepted)*, vol. 23, no. 8, pp. 10072–10090, 2024.

[17] T. Kaiser, F. Zheng, and E. Dimitrov, "An overview of ultra-wide-band systems with MIMO," *Proc. IEEE*, vol. 97, no. 2, pp. 285–312, 2009.

[18] D. S. Kumar, I. S. Hinduja, V. V. Mani, and R. Bose, "Beamforming of ultra wideband signals in an IEEE 802.15.3a channel environment," in *2014 IEEE Int. Conf. on Ultra-WideBand (ICUWB)*, pp. 41–46, 2014.

[19] S. B. Venkatakrishnan, D. K. Papantonis, A. A. Akhiyat, E. A. Alwan, and J. L. Volakis, "Experimental validation of on-site coding digital beamformer with ultra-wideband antenna arrays," *IEEE Trans. Microw. Theory Tech.*, vol. 65, no. 11, pp. 4408–4417, 2017.

[20] M. Naseri, A. Shahid, G.-J. Gordebeke, S. Lemey, M. Boes, S. Velde, and E. Poorter, "Machine learning-based angle of arrival estimation for ultra-wide band radios," *IEEE Commun. Lett.*, vol. 26, no. 6, 2022.

[21] I. Dotlic, A. Connell, H. Ma, J. Clancy, and M. McLaughlin, "Angle of arrival estimation using decawave DW1000 integrated circuits," in *2017 14th Workshop Position. Navigation Commun. (WPNC)*, 2017.

[22] F. Ma, J. He, and X. Zhang, "Robust kalman filter algorithm based on generalized correntropy for ultra-wideband ranging in industrial environment," *IEEE Access*, vol. 7, pp. 27490–27500, 2019.

[23] W. Wang, D. Marelli, and M. Fu, "Multiple-vehicle localization using maximum likelihood kalman filtering and ultra-wideband signals," *IEEE Sensors J.*, vol. 21, no. 4, pp. 4949–4956, 2021.

[24] IEEE Computer Society, "IEEE standard for low-rate wireless network-samendment 1: Enhanced ultra wideband (UWB) physical layers (PHYs) and associated ranging techniques," *IEEE Standard 802.15.4z*, 2020.

[25] IEEE Computer Society, "IEEE standard for low-rate wireless networksamendment 1: Enhanced ultra wideband (UWB) physical layers (PHYs) and associated ranging techniques," *IEEE Standard 802.15.4z-2020 (Amendment to IEEE Std 802.15.4-2020)*, 2020.

[26] Samsung Electronics Co., Ltd., "Samsung expects UWB to be one of the next big wireless technologies," *[Online]. Available: https://news.samsung.com/global/samsung-expects-uwb-to-be-one-of-the-next-big-wireless-technologies*.

[27] Apple Inc., "Ultra wideband security in ios," *[Online]. Available: https://support.apple.com/guide/security/ultra-wideband-security-sec1e6108efd/web*.

[28] Car Connectivity Consortium, "CCC digital key - the future of vehicle access," *[Online]. Available: https://carconnectivity.org/wp-content/uploads/2022/11/CCC_Digital_Key_Whitepaper_Approved.pdf*.

[29] FiRa Consortium, "Technical specifications," *[Online]. Available: https://www.firaconsortium.org/certifications/technical-specifications*.

[30] C. Sturm and W. Wiesbeck, "Waveform design and signal processing aspects for fusion of wireless communications and radar sensing," *Proc. IEEE*, vol. 99, no. 7, pp. 1236–1259, 2011.

[31] H. Hawkins, C. Xu, L.-L. Yang, and L. Hanzo, "IM-OFDM ISAC outperforms OFDM ISAC by combining multiple sensing observations," *IEEE Open J. Veh. Technol.*, vol. 5, pp. 312–329, 2024.

[32] L. Gaudio, M. Kobayashi, G. Caire, and G. Colavolpe, "On the effectiveness of otfs for joint radar parameter estimation and communication," *IEEE Trans. Wireless Commun.*, vol. 19, no. 9, pp. 5951–5965, 2020.

[33] Z. Li, W. Zou, B. Li, Z. Zhou, and X. Huang, "Analysis on coexistence of ultra wideband with OFDM-based communication systems," *IEEE Trans. Electromagnetic Compatibility*, vol. 53, no. 3, pp. 823–830, 2011.

[34] A. Batra, J. Balakrishnan, G. R. Aiello, J. R. Foerster, and A. Dabak, "Design of a multiband OFDM system for realistic UWB channel environments," *IEEE Trans. Microw. Theory Tech.*, vol. 52, no. 9, pp. 2123–2138, 2004.

[35] Y. Zhang, F. Liu, and T. Zhang, "Decoupling strategies for asynchronous integrated communication and localization networks," in *2023 IEEE 98th Veh. Technol. Conf. (VTC2023-Fall)*, 2023.

[36] X. Wang, F. Liu, Z. Zhang, and T. Zhang, "Fundamental limits on joint delay and doppler characterization in UWB ISAC systems," in *2023 IEEE 98th Veh. Technol. Conf. (VTC2023-Fall)*, pp. 1–6, 2023.

[37] J. Chen, X. Wang, F. Liu, Z. Zhang, J. Xue, and T. Zhang, "Differential decoupling strategies for uwb integrated sensing and communication systems," in *2023 IEEE Veh. Technol. Conf. (VTC2023-Fall)*, 2023.

[38] Z. Zhang, F. Liu, and T. Zhang, "Fundamental limits on integrated sensing and communications frameworks: An IR-UWB case," in *ICC 2023 - IEEE Int. Conf. Commun.*, pp. 2729–2734, 2023.

[39] F. Liu, T. Zhang, Z. Zhang, Y. Shen, and Q. Zhang, "ISAC with UWB: Reliable decoupling and target sensing," *IEEE Trans. Wireless Commun.*, vol. 23, no. 11, pp. 15957–15972, 2024.

[40] K. Witrisal, G. Leus, G. Janssen, M. Pausini, F. Troesch, T. Zasowski, and J. Romme, "Noncoherent ultra-wideband systems," *IEEE Signal Process. Mag.*, vol. 26, no. 4, pp. 48–66, 2009.

[41] L. Yang, G. Giannakis, and A. Swami, "Noncoherent ultra-wideband (de)modulation," *IEEE Trans. Commun.*, vol. 55, pp. 810–819, 2007.

[42] F. Wang, Z. Tian, and B. Sadler, "Weighted energy detection for noncoherent ultra-wideband receiver design," *IEEE Trans. Wireless Commun.*, vol. 10, no. 2, pp. 710–720, 2011.

[43] C. Xu, Y. Xiong, N. Ishikawa, R. Rajashekar, S. Sugiura, Z. Wang, S. X. Ng, L.-L. Yang, and L. Hanzo, "Space-, time- and frequency-domain index modulation for next-generation wireless: A unified single-/multi-carrier and single-/multi-RF MIMO framework," *IEEE Trans. Wireless Commun.*, vol. 20, no. 6, pp. 3847–3864, 2021.

[44] N. Ishikawa, S. Sugiura, and L. Hanzo, "50 years of permutation, spatial and index modulation: From classic RF to visible light communications and data storage," *IEEE Commun. Surveys Tut.*, vol. 20, no. 3, pp. 1905–1938, 2018.

[45] S. Sugiura, T. Ishihara, and M. Nakao, "State-of-the-art design of index modulation in the space, time, and frequency domains: Benefits and fundamental limitations," *IEEE Access*, vol. 5, pp. 21774–21790, 2017.

[46] Decawave, "DW3000 family user manual," *[Online]. Available: https://www.decawave.com/product/decawave-dw3000-ic/*.

[47] C. Xu, S. Sugiura, S. X. Ng, P. Zhang, L. Wang, and L. Hanzo, "Two decades of MIMO design tradeoffs and reduced-complexity MIMO detection in near-capacity systems," *IEEE Access*, vol. 5, pp. 18564–18632, 2017.

[48] S. X. Ng and L. Hanzo, "On the MIMO channel capacity of multidimensional signal sets," *IEEE Trans. Veh. Technol.*, vol. 55, pp. 528–536, Mar. 2006.